Identifying and Constraining Marsh-Type Transitions in Response to Increasing Erosion over the Past Century

Alisha M. Ellis[1] · Christopher G. Smith[1] · Kathryn E. L. Smith[1] · Jessica A. Jacobs[1]

Abstract

Marsh environments, characterized by their flora and fauna, change laterally in response to shoreline erosion, water levels and inundation, and anthropogenic activities. The Grand Bay coastal system (USA) has undergone multiple large-scale geomorphic and hydrologic changes resulting in altered sediment supply, depositional patterns, and degraded barrier islands, leaving wetland salt marshes vulnerable to increased wave activity. Two shore-perpendicular transect sites, one along a low-activity shoreline and the other in a high activity area of the same bay-marsh complex, were sampled to investigate how the marshes within 50 m of the modern shoreline have responded to different levels of increased wave activity over the past century. Surface sediments graded finer and more organic with increased distance from the shoreline while cores generally exhibited a coarsening upwards grain-size trend; all cores contained multiple large sedimentological shifts. ^{210}Pb-based mass accumulation rates over the last two decades were greater than the long-term (centurial) average at each site with the fastest accumulation rates of 7.81 ± 1.58 and 7.79 ± 1.63 kg/m^2/year at the sites nearest the shoreline. A shoreline change analysis of three time-slices (1848–2017, 1957–2017, 2016–2017) shows increased erosion at both sites since 1848 with modern rates of -0.95 and -0.88 m/year. Downcore sedimentology, mass accumulation rates, and shoreline change rates paired with foraminiferal biofacies and identification of local estuarine indicator species, *Paratrochammina simplissima*, aided in identifying paleo marsh types, their relative proximity to the shoreline, and sediment provenance. The high-energy marsh site transitioned from middle marsh to low marsh in the 1960s, and the low-energy marsh site transitioned later, at the end of the twentieth and early twenty-first century, due to its more protected location. Marsh type transition corresponds chronologically with the coarsening upwards grain-size trend observed and the degradation of Grand Batture Island; since its submergence, signatures of multiple storm event have been preserved downcore.

Keywords Marsh sediments · Marsh foraminifera · Geochronological data · Shoreline change rates · Coastal change

Introduction

Salt marshes are found globally in subtropical and temperate climates along microtidal to macrotidal low-energy coasts (Allen and Pye 1992) and offer essential ecosystem services by protecting inland communities and property from storms, sequestering carbon, and providing wildlife habitats. Marsh loss affects coastal systems around the world and is driven by a variety of stressors, including changes in sea-level, sediment availability, climate, and anthropogenic activities (Phillips 1986; Schwimmer 2001; McClenachan et al. 2013; among others). Common hydrologic and geomorphic responses to these drivers are alterations in wave energy and shoreline exposure to wave activity which can increase shoreline erosion and marsh loss. Marsh resilience to erosion is dependent on feedbacks between physical (e.g., hydrology, sediments, and morphology) and biogeochemical (e.g., plant production and decomposition, and organisms) processes (Wilson et al. 2021) but has largely been attributed to wave attack (Leonardi et al. 2016; Sanford and Gao 2018). Although shoreline-change rates for the past 50–100 years are commonly measured using historic maps and remote sensing (Burningham and Fernandez-Nunez 2020), records prior to the 1980s are geographically limited, have

✉ Alisha M. Ellis
aellis@usgs.gov

1   U.S. Geological Survey, St. Petersburg Coastal and Marine
    Science Center, 600 4th Street South, St. Petersburg,
    FL 33701, USA

large spatial error, and do not provide information on changing marsh conditions and interactions.

Over decadal to centennial timescales, downcore sedimentology and sediment-derived geochronologies can provide insights into marsh sediment provenance and accumulation rates while shoreline erosion rates may be calculated using modern (field collected) and historical shoreline positions. Marsh cores may exhibit steady trends or gradational changes in organic matter (OM) content and grain size due to autochthonous production and allochthonous deposition, which may vary temporally in the core due to changing sediment sources, plant production, and hydrodynamics (Belknap and Kelley 2021). Episodic events (e.g., hurricanes) can also be evident in marsh cores, often as sharp or erosional contacts, though sedimentary signatures of those deposits tend to be more variable due to characteristics such as estuarine sediment type, marsh and upland sediment type, ebb or flood tides, and event features such as wave heights, extent of inland flooding, and distance from the shoreline (Liu and Fearn 1993; Hawkes and Horton 2012; Yao et al. 2018). With the use of an appropriate standard analytical age-model, utilizing ^{210}Pb and ^{137}Cs activity data from sediment core samples, linear sedimentation rates (LSR) and mass accumulation rates (MAR) can be determined, and sedimentological shifts and episodic events can be temporally constrained (DeLaune et al. 1989; Chmura et al. 2001). Modern and historically derived shoreline positions, and the linear regression rates calculated from them, can aid in sedimentological interpretations by providing information on site location relative to the shoreline, shoreline change rates, the evolution of geomorphic features in the region, and geomorphic impacts of storm events (e.g., erosion, breach; Dolan et al. 1991; Fenster et al. 2001).

Microfossils are commonly used to examine modern and past geologic and hydrodynamic processes and conditions due to their environmental preferences in marshes, estuaries, and oceans (such as salinity and water level; Gehrels and Kemp 2021). Benthic foraminifera microfossils, common in coastal sedimentary records, are useful environmental indicators due to their habitat preferences, relatively short lifespans, small-size, and high preservation potential. Marsh species exhibit preferences towards salinity and inundation or tidal flooding frequency which are reflective of elevation relative to mean sea level and vegetation zones (Scott 1976; Scott and Medioli 1978, 1980; Edwards and Wright 2015), and sediment properties (Debenay et al. 2001; Diz et al. 2004; Armynot du Châtelet et al. 2009). When paired with downcore sedimentology, sediment-derived geochronologies, and historically derived shoreline positions, preserved foraminiferal assemblages are useful proxies for paleoenvironmental conditions (e.g., salinity, marsh-type, estuarine incursion, event layers) that may not be otherwise apparent or well-defined based on sediment characteristics alone.

The ability to examine changes in marsh conditions due to factors like shoreline erosion provides information on the interactions and feedbacks between sediments and hydrology, which can be used to integrate ecological response into models that predict marsh resilience to future changes.

The goals of this study are to use modern and recent sedimentological changes and foraminiferal biofacies downcore and across shore-proximal marsh transects to (1) identify and distinguish marsh facies, (2) examine the influence of shoreline dynamics on the evolution of the shore-proximal marsh facies and transitions, and (3) evaluate the architecture and evolution of the marsh facies through time to understand how regional controls (e.g., accommodation, sediment supply, regional landscape changes, and/or events), influenced the marsh response. The undeveloped, protected, and managed federal and state Grand Bay (GB) system—a national estuarine research reserve comprised of a number small, interconnected bays (e.g., Grand and Middle Bays) on the border of Mississippi (MS) and Alabama (AL, USA; Fig. 1A–C)—serves as an idealized, natural laboratory to examine marsh response to changing sediment supply and accommodation.

Geologic Setting

During the late Holocene, the northern Gulf of Mexico coastal system experienced numerous natural landscape changes succeeding geomorphic, hydrologic, and environmental alterations in response to sea level rise and hurricane activity (Eleuterius and Criss 1991; Davies and Hummell 1994; Hollis et al. 2019). The Escatawpa River (MS and AL; Fig. 1B) avulsion diverted sediment away from GB to Pascagoula River which ended the supply and seaward transport of fluvial sediment that offset eroded sediment volumes (Eleuterius and Criss 1991). The reworked delta lobe sediments were redistributed following the Escatawpa River avulsion and formed baymouth bars known as the Grand Batture Islands (Fig. S2), which sheltered Grand and Middle Bay from northerly directed waves. The creation of Petit Bois Pass in 1740 by a hurricane dissecting Dauphin Island resulted in larger waves in Mississippi Sound (Fig. 1B) and increased tidal energy, which caused increased fair-weather erosion (Eleuterius and Criss 1991). The Grand Batture Islands (Fig. S2) were continuously reduced by both fair-weather erosion and storm events and became a submerged sand shoal by 1969 following Hurricane Camille (Eleuterius and Criss 1991). Over the last 200 years, railroads, highways, and cultivated lands across the relict Escatawpa River channel have further isolated the GB system by restricting sediment and freshwater inputs (Gazzier 1977; Davies and Hummell 1994). Morton (2008) suggested that dredging and maintenance of inlets/shipping channels altered the natural sediment budget of the MS-AL barrier island system which coincided with losses in barrier island area.

Fig. 1 **A** Location map of Grand Bay along the northern Gulf of Mexico coastline; **B** regional map of the Grand Bay system in southern Mississippi (MS) and Alabama (AL); **C** location of transect Sites 1 and 3, on opposite sides of Middle Bay, with a thin, nearly vertical dashed line indicating the MS and AL state border and a thicker, closely spaced dashed line indicating the approximate location of Grand Batture Island in 1848; and **D** and **E** are elevation profiles (in meters, NAVD88) for each sample transect at Site 1 and Site 3, respectively; y-axis is vertically exaggerated; location of shoreline is indicated with vertical black line at 0 along the x-axis. All land shown on the MS side of the state line in (C) is part of the Grand Bay National Estuarine Research Reserve (NERR); digitized and geo-rectified NOAA t-sheet from 2007 was used for the shoreline (Buster and Morton 2011). On parts **D** and **E**, marsh cores (Site 1, white squares; Site 3, white circles) and surface sample (Site 1, black squares; Site 3, black circles) transects are plotted and extend from +50 m inland to 10 m into the estuary (−10). Mean higher-high water (MHHW) is indicated at 0.302 m by the horizontal dashed and dotted line and mean sea level (MSL) is indicated at 0.059 m by the horizontal short-dashed line relative to NOAA station 8740166 located in Grand Bay NERR, Mississippi Sound, MS
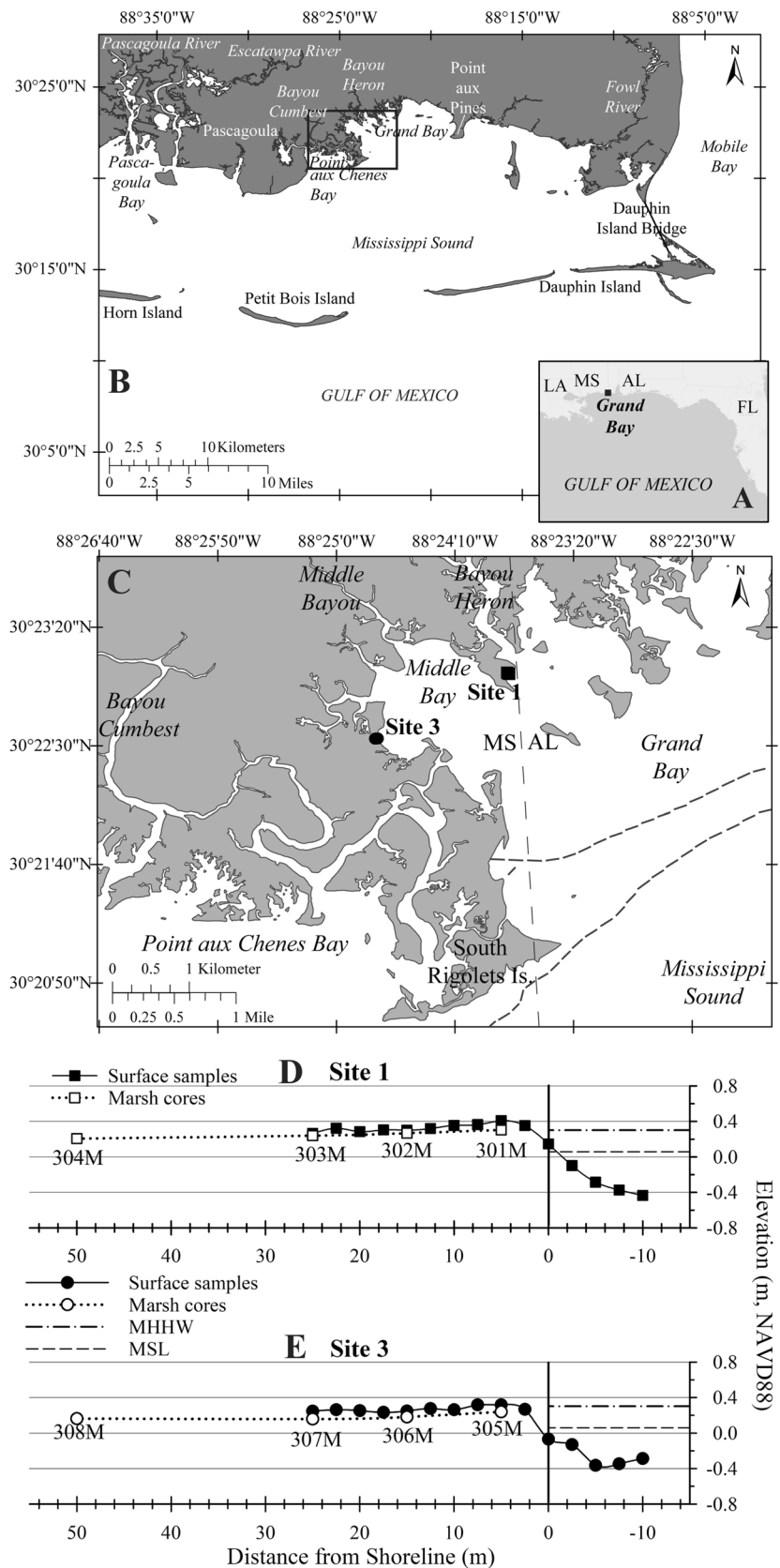
The GB marsh-estuarine system formed on an abandoned deltaic system, with the modern marshes overlying relict distributary channels, levees, and lobes and the modern, wind-dominated, microtidal estuaries occupying former interdistributary bays (Kramer 1990). Average diurnal tidal amplitude is 0.42 m. Most winds originate from the north though the strongest winds (> 10 m/s) blow from the south and southeast (Fig. S1). Wind activity increases in the late summer and winter, amplifying the tides and generating significant wave heights (e.g., 0.3 m) in the bays resulting in high suspended sediment concentrations (SSC; > 100 mg/L; Nowacki and Ganju 2020). Recent studies have implicated the submergence of the Grand Batture Islands over the last 100 years as a major contributor to the evolution of the Grand Bay system into an erosional (Wacker and Criss 1996; Terrano 2018; Smith et al. 2021a), ebb-dominated, microtidal bay (Passeri et al. 2015) where suspended sediment export exceeds import (Nowacki and Ganju 2019). Despite the overall export of sediment out of the estuary, depositional fluxes onto the marsh surface proximal to the shoreline balance erosional fluxes released by shoreline erosion (Smith et al. 2021a). Recent foraminiferal biofacies work conducted in the area (1) catalogued the modern distribution, (2) characterized the assemblages, (3) evaluated taphonomic loss, and (4) explored the impacts of the submergence of the Grand Batture Islands, anthropogenic activities, and storm events over the last century by analyzing subsurface samples (Osterman and Smith 2012: Mobile Bay, AL; Haller et al. 2019: GB, MS, AL, Pascagoula Bay, MS, Dauphin Island, AL, and Fowl River, AL; Ellis and Smith 2021: GB, MS, AL).

Field and Laboratory Methods

Sampling Strategy

Two 50-m long, shore-perpendicular marsh transect sites, identified as Sites 1 and 3, were established on opposite sides of Middle Bay (Fig. 1C) to assess depositional trends laterally and vertically. Both sites are frequently inundated though Site 1, which is more exposed, receives more direct wave activity from the south due to increased fetch across the bay compared with Site 3, located along a more protected, low-energy shoreline subject to less wave activity (Fig. 1; Table S1). The relative amounts of wave activity each site experiences led to the designation of Site 1 as a higher-energy shoreline and Site 3 as a low-energy shoreline in agreement with Smith et al. (2021a). Site 1 and 3 shorelines were fringed by sparse *Spartina alterniflora* (Loisel) and dominated by *Juncus roemerianus* (Scheele). Four sediment push cores and a set of 15 surface sediment samples were collected along parallel transects at each site

(Fig. 1D, E). Cores were collected at distances of 5, 15, 25, and 50 m from the shoreline while surface samples were collected every 2.5 m starting at 25-m landward of the shoreline extending 10 m into the estuary along with location data (Fig. 1D, E). Elevation profiles at both sites had a relatively steep shoreface at the marsh edge, a berm-like feature just landward of the shoreline, and a nearly flat platform landward of the berm. The elevation of the berm crest at Sites 1 and 3 were 0.41 m (NAVD88) and 0.32 m, respectively, and were located at 5 and 7.5-m inland of the shoreline, respectively. The slope from the shoreline to berm crest at both sites increased at a similar rate (0.05 m/m) while the slope in elevation landward of the berm crest was steeper at Site 3 (−0.02 m/m) than Site 1 (−0.01 m/m). No samples were collected in the high marsh or upland for this study which focused on depositional trends within 50 m of the estuarine shoreline unlike Haller et al. (2019) and sea-level studies (Edwards and Wright 2015).

Surface samples were collected by scraping the top 1 cm of sediment from the marsh or estuarine surface within an approximate 15-cm diameter. Cores were pushed into the marsh by hand to reduce compaction, quantified measuring distance to the marsh surface (~1-cm resolution) inside and outside of the core barrel. Cores were vertically extruded and sectioned into 1-cm intervals ($N = 374$) following the procedure of Osbourne and DeLaune (2013). Core 304 M had low viscosity, unconsolidated sediment at the core top; therefore, this unconsolidated sediment was collected and labeled "top" prior to the collection of the more consolidated 0–1-cm core sediment sample; the core "top" was assessed with all 0–1-cm intervals resulting in nine "surficial" core samples. Each 1-cm interval was subsampled for grain-size and foraminiferal microfossil analysis (stored wet and refrigerated, foraminiferal subsample was stored without a cytoplasm stain such as rose Bengal) and for physical sediment characteristics and chronologies via radiochemistry. For additional and more detailed descriptions of the field and laboratory procedures used refer to Supplemental Methods, Smith et al. (2013), Marot et al. (2019), Ellis et al. (2021), and Ellis et al. (2022).

Laboratory and Data Analyses

Sedimentological Analyses

For each of the physical sediment characteristic core subsamples, the wet subsample volume and mass were measured then dried at 60 °C (> 48 h), the dry mass was measured, and the dry subsample was pulverized and homogenized. Dry bulk density (DBD, g/cm^3) was estimated as the final dry weight divided by the measured wet volume. All surface samples were dried at 60 °C without DBD measurements

(details provided in Supplemental Methods). OM content was measured on a portion of the dried core subsamples and the surface samples using loss-on-ignition (LOI), which reflects the mass lost from dry sediment (110 °C) after being combusted for 6 h at 550 °C in a muffle furnace relative to the initial dry sediment mass (Galle and Runnels 1960; Dean 1974). Select core-intervals ($n = 96$) and all surface samples ($n = 30$) were analyzed for grain-size distribution; core intervals were selected to capture variations in sediment-types based on DBD and LOI values. Prior to particle-size analysis, wet sediment subsamples were digested with hydrogen peroxide (Poppe et al. 2000) then analyzed with replication on a Coulter LS 13 320 particle-size analyzer. Particle size data for each sample was processed and averaged using GRADISTAT (v. 8; Blott and Pye 2001) to generate grain-size metrics (e.g., mean grain-size, sorting, and percent clay; details provided in Supplemental Methods).

Gamma Spectrometry and Geochronometry Methods

Each 1-cm interval from the top 30 cm from every core, every-other-cm from 30 cm to the core base ($n = 306$) and select dry, homogenized surface samples ($n = 19$) were analyzed by standard gamma-ray spectrometry on low energy, high purity germanium detectors (Cutshall and Larsen 1986) to measure the specific activity, in disintegrations per minute per gram (dpm/g), of lead-210 (^{210}Pb), cesium-137 (^{137}Cs), and radium-226 (^{226}Ra) via radon-222 (^{222}Rn) progeny radioisotopes lead-214 (^{214}Pb), and bismuth-214 (^{214}Bi). Samples were sealed in air-tight containers and stored for at least 3 weeks prior to analysis, permitting secular equilibrium between ^{226}Ra and ^{214}Pb and ^{214}Bi. Sample count rates were corrected for detector efficiency, standard photopeak intensity, and self-absorption using an International Atomic Energy Agency RGU-1 uranium-238 (^{238}U) sealed source (planar detectors only; Cutshall et al. 1983).

Specific activities of ^{210}Pb (half-life, $t_{1/2} = 22.3$ years, y), ^{226}Ra ($t_{1/2} = 1600$ y), and ^{137}Cs ($t_{1/2} = 30.2$ y) were used to evaluate sediment depositional patterns downcore and with distance from the shoreline. Given the proximity of the cores at each site (i.e., within 50 m of each other), comparisons were made with core-tops and surface sediment activities. Disequilibrium between ^{210}Pb and ^{226}Ra is determined by the difference in total activity (i.e., ^{210}Pb$_{xs}$ = ^{210}Pb$_{tot}$ − ^{226}Ra, where "xs" denotes excess, "tot" denotes total, and ^{226}Ra is roughly equivalent to supported ^{210}Pb; ^{210}Pb$_{sup}$). At the surface, disequilibrium is presented as an activity ratio (AR) of progeny-to-progenitor (^{210}Pb$_{total}$/^{226}Ra or ^{210}Pb$_{total}$/^{210}Pb$_{sup}$), used to investigate surface sediment provenance. AR values of approximately 1 indicates sediment ^{210}Pb$_{total}$/^{226}Ra activities are in or near secular equilibrium; a greater AR indicates adsorption of ^{210}Pb from atmospheric fallout onto fine-grained and organic sediments. Other factors that may impact AR values include dilution due to coarse-grained sediment and winnowing of fine-grained particles.

For each core, an age-depth relationship was determined using geochronologic models of downcore ^{210}Pb$_{xs}$ and corroborated with profiles of ^{137}Cs activity (following Smith et al. 2013). Initially, downcore profiles of both geochronometers were assessed relative to the "ideal" form; for ^{210}Pb$_{xs}$, this is a monotonic, exponentially decreasing profile that terminates at or near 0 (i.e., secular equilibrium between ^{210}Pb$_{tot}$ and ^{210}Pb$_{sup}$). The ideal form for ^{137}Cs is a mid-depth maximum, reflecting peak atmospheric activity/flux of 1963 with slight diffusional characteristics above and below the peak, a reflection of the 20+ years of atmospheric nuclear testing and residence time of ^{137}Cs in the atmosphere (Robbins and Edgington 1975; Chmura and Kosters 1994; Milan et al. 1995). Depth-integrated inventories were computed for each radionuclide using specific activity and sediment dry bulk density; inventories were compared among the core set and with literature-based regional values (Smith et al. 2013 and references therein; Marot et al. 2019; Ellis and Smith 2021).

Three geochronologic models were considered and initially tested, utilizing ^{210}Pb$_{xs}$ activities to provide age-depth results that were compared with ^{137}Cs profiles. Each model carries a name that reflects the assumption the model makes with respect to supply and burial of ^{210}Pb$_{xs}$ (Corbett and Walsh 2015): (1) constant-flux, constant sedimentation or CFCS, (2) constant initial concentration CIC, and (3) constant rate of supply or CRS. The data assessments outlined above (surface activities, activity-depth profile shape, and inventories) were compared with the inherent assumptions of the three models. Based on these collective assessments, the CRS model was considered the most applicable and valid.

The CRS model assumes that the supply or flux of ^{210}Pb$_{xs}$ to the sediment surface, which is incorporated into the sediment column, is constant, allowing for inverse variations in accumulations rate and ^{210}Pb$_{xs}$ activities through time; this model was determined to be the most appropriate model for the environment (Goldberg 1963; Appleby and Oldfield 1978; Binford 1990). Geochronology development followed the detailed procedure outlined by Smith et al. (2013: Mobile Bay, AL). Mass accumulation rates (MAR, in kilograms per square meters per year kg/m^2/year) and age-depth (year-cm) relationships for the last approximately 120 years (five ^{210}Pb half-lives) were calculated from linear sedimentation rates (LSR, in centimeters per year, cm/year) using DBD and LOI values to calculate mass depth (in g/cm^2) and assess organic versus inorganic accumulation rates (g/cm^2/year), respectively. Due to inherent increased error in age-depth relationships with depth (Binford 1990), we only utilized the stratigraphic record with modeled age-depths later than 1916 (100 years prior to sampling) unless otherwise stated. Decadal averages were calculated using age-depths for 13-year

windows (i.e., 10 ± 1.5 year, therefore the ages utilized for the 1990–2000 decadal average are 1988.5–2001.5).

Foraminiferal Processing Methods and Analyses

Select refrigerated wet 1-cm interval core subsamples were processed for foraminifera ($n = 69$). Interval selections were based on fluctuations in downcore DBD, LOI, and grain-size to capture both "background" and potential event sediments. For each foraminiferal subsample, approximately 20 ml of sediment was gently agitated on a shaker plate in a beaker with tap water prior to being wet sieved over a 63 and 500 µm sieve stack or a 63, 125, and 500 µm sieve stack and dried at 40 °C (see Supplemental Methods for explanation). Dry sediment was split into equal parts with a micro-splitter, spread over a gridded picking tray, and entire splits were picked from 125 to 500 µm fraction under a binocular dissecting microscope until at least 200 specimens were acquired. Identifications were made by making comparisons with published literature (Edwards and Wright 2015; Haller et al. 2019) and through consultation and specimen identification comparisons.

A principal component analysis (PCA) was performed in Canoco5 (Smilauer and Leps 2014) on the seven upper-most core intervals (0–1 cm for six of eight cores; 304 M used 1–2 cm; 307 M does not have microfossil data) using the six most dominant species (*Ammotium* cf. *A. salsum*, *Arenoparella mexicana*, *Haplophragmoides wilberti*, *Miliammina fusca*, *Trochammina inflata*, and *Tiphotrocha comprimata*) and *Paratrochammina simplissima*, a local estuarine deposition indicator species (Ellis and Smith 2021), in conjunction with site ID, elevation, distance from shoreline, percent OM, and median grain-size. Primer7 (v. 7.0.13; Clarke and Gorley 2015) was used to perform an analysis of similarities (ANOSIM) with a Bray-Curtis similarity index on square root transformed abundance core data with transect location (1, 3), distance from the shoreline (5, 15, 25, 50 m), and core depth. Downcore foraminiferal assemblages were identified using a hierarchical cluster analysis with a Bray-Curtis similarity index on square root transformed abundance data in Primer7. Cluster results were compared with a non-metric multi-dimensional scaling (NMDS) analysis (Primer7) with 2-dimensional and 3-dimensional Bray-Curtis similarity plots on the square root transformed abundance data. Fisher's alpha (α) diversity index was computed in PAST (Hammer et al. 2001) for all samples and averaged for all cluster groups; Fisher's α is a function of density (N, number of specimens per sample per 1 ml) and species richness (*S*, number of species per sample per 1 ml). Pearson correlations were performed in Excel on a variety of species, radiochemical, sedimentological, and environmental parameter combinations.

The results of these multivariate analyses were compared with previous studies that examined foraminiferal assemblages from multiple marsh (Haller et al. 2019) and estuarine environments (Phleger 1954; Lamb 1972; Osterman and Smith 2012; Ellis and Smith 2021) within the coastal zone of Mississippi and Alabama (USA), including Grand Bay (i.e., Haller et al. 2019; Ellis and Smith 2021). Haller et al. (2019) categorized the northern Gulf of Mexico biofacies into (1) estuary, (2) low salinity, (3) low marsh, (4) middle marsh, (5) high marsh, and (6) upland transition, identifying dominant (> 5% abundance) and characteristic species, as classified by a biofacies fidelity, constancy, and occurrence (BFCO) analysis, for each biofacies (Table 1). Relevant findings that aided in interpretation of results in this study include (1) the emergence of *P. simplissima* (Table S2: species abbreviations)—a shallow shelf agglutinated species that has been identified in Mobile Bay, GB estuary, and Pascagoula Bay (Osterman and Smith 2012; Haller et al. 2019; Ellis and Smith 2021), (2) the reduction in calcareous taxa in Mobile Bay (Osterman and Smith 2012), and (3) the increase in calcareous taxa in GB estuary (Haller et al. 2019).

Shoreline Change Rate Methods

Shoreline-change rates using historical charts and t-sheets, aerial imagery, and field-collected GPS and dGPS data were calculated using the AMBUR (Analyzing Moving Boundaries Using R) statistical package for R (v. 3.4.3). The AMBUR package provides tools to create cross-shore transects that intersect vector-based shorelines and estimate shoreline change rate by calculating the linear regression rates of shoreline movement (distance) landward or seaward over time in meters/year. For this study, shoreline-change rate averages were calculated for Sites 1 and 3 using ten and six transects, respectively, for three time periods and referred to as (1) modern shoreline-change rate (October 2016–October 2017), (2) short-term shoreline-change rate (1957–October 2017), and (3) long-term shoreline-change rate (1848–October 2017). Historical shorelines, field methods, uncertainty estimates, data processing, and shoreline change analysis methods are described and published in the Supplemental Methods, Terrano (2018), and Terrano et al. (2019) and Smith et al (2021b).

Results

Marsh Sedimentology

To examine the influence of shoreline dynamics on the marsh sedimentary record laterally and vertically, surficial and downcore samples were assessed for textural and OM gradients. Surface sediment grain-size generally fined in a landward direction. The core tops and marsh surface samples ("top" for 304 M; $n = 9$) at the 5-m sites exhibited the greatest percent sand content (81.7% and 72.9%) compared

Table 1 Proportions of dominant live and dead species for each assemblage, and the characteristic species (numbers in **bold** font) for each assemblage, as determined using a biofacies fidelity and constancy (BFCO) analysis, identified in Haller et al. (2019) for five major environments along the northern Gulf of Mexico: estuary, low marsh, middle marsh, high marsh, and upland transition. Species abbreviations utilized throughout the table are available in Table S2. Dashes indicate absence of that species in the specified environment

Benthic species	Estuary		Low marsh		Middle marsh		High marsh		Upland transition	
	Live	Dead	Live	Dead	Live	Dead	Live	Dead	Live	Dead
Calcareous species										
Am. parkinsoniana	-	7	-	-	-	-	-	-	-	-
Am. tepida	**49**	64, 17	7	-	7	-	-	-	-	-
Cr. excavatum	**5**	**20, 3**	-	-	-	-	-	-	-	-
Cr. poeyanum	**1**	**2**	-	-	-	-	-	-	-	-
Hy. germanica	**6**	**0.9**	3	-	-	-	-	-	-	-
Miliolinella subrotunda	-	**2**	-	-	-	-	-	-	-	-
Agglutinated species										
A. salsum	18	52, 3	53	41	13	13, 6	-	-	-	-
Ammoastuta inepta	-	-	-	-	8	-	-	-	-	-
Ar. mexicana	-	-	-	-	**26**	36, 16	-	-	-	-
E. macrescens	-	-	-	-	-	-	-	81	-	25
H. manilaensis	-	-	-	-	-	-	-	-	-	**14**
H. wilberti	-	-	-	-	-	22	-	-	73	5
M. fusca	-	9	25	41	21	28, 9	-	-	-	-
M. petila	-	-	-	-	-	-	-	**3**	-	-
P. simplissima	**14**	**10**	-	-	-	-	-	-	-	-
Ps. limnetis	-	-	-	-	-	-	-	-	22	79, 16
S. lobata	-	-	-	-	-	-	-	7	**3**	-
T. inflata	-	-	-	-	**10**	10, 13	-	-	-	-
Ti. comprimata	-	-	-	-	**5**	17	-	4	-	-
Trochamminita irregularis	-	-	-	-	-	-	-	-	-	**39, 4**

with the 15–50-m sites (Fig. S3). The 5-m sites consisted of very fine sand (d50 = 100.9 and 82.1 μm), and little OM (2.3% and 3.2%). As distance from the shoreline increased, percent OM generally increased with a maximum percent OM of 14.2% and 14.8% at the 25-m sites. Both 25-m sites also contained the highest percent mud (mud = silt + clay fraction; 86.0% and 76.7%) and finest d50 (coarse silt; 21.3 and 20.6 μm). The 50-m sites exhibited a slight increase in d50 (304 M top, 47.6 μm; 304 M 0–1 cm, 71.3 μm; 308 M, 37.4 μm) and decrease in percent OM (304 M top, 12.7%; 304 M 0–1 cm, 8.0%; 308 M, 14.5%) compared to the 25-m sites (Fig. S3).

Core sediment samples (*n* = 96) were moderately to very poorly sorted; d50 varied between a medium silt and very fine sand (20.5–126.6 μm), and percent sand ranged from 14.0 to 81.7%. All cores exhibited one or more large shifts in percent sand/mud (> 25%) over a depth range of ≤ 5 cm; these shifts occurred six times in cores collected from Site 1, along the high energy shoreline, and nine times in cores collected from Site 3, the more protected shoreline (Fig. 2). The largest sedimentological shift occurred in 301 M (Site 1 5-m core) which exhibited a 59.4% shift in percent mud from 16–17 to 21–22-cm depth (Fig. 2). Downcore, percent OM ranged from 2.2 to 28.0%; OM core averages and ranges generally increased inland along each marsh transect with

distance from the shoreline (Fig. 2). Percent OM exhibited the strongest relationship with percent clay (*r* = 0.75) compared to other sedimentological parameters.

Sediment Radiochemistry: Patterns and Activities

The AR of surface sediment samples (including core tops) varied spatially at both sites and exhibited similar patterns. Marsh sediment AR increased inland with distance from shoreline while estuarine surface sediments were nearly constant and equilibrated (AR ~ 1) with no qualitative or quantitative pattern relative to the shoreline (Fig. 3). At both sites average ARs from the estuary to 5-m inland were 1.4 while ARs ranged from 3.2 to 6.0 at 25 m (M = 4.75; Fig. 3). Beyond 25 m, the AR for each transect decreased but were collectively within the range observed at 25 m (Fig. 3). As expected, correlations of surficial AR with percent silt, clay, and OM exhibit strong relationships (silt, *r* = 0.74; clay, *r* = 0.77; and OM, *r* = 0.96).

Downcore profiles of total ^{210}Pb and the natural log (ln) of ^{210}Pb$_{xs}$ activity varied across the transects (Fig. 4; Fig. S4). At both 5-m sites, ^{210}Pb activity profiles were nearly vertical and had only slight linear-slopes such that secular equilibrium occurred at 34–38 cm (Fig. 4). Activity
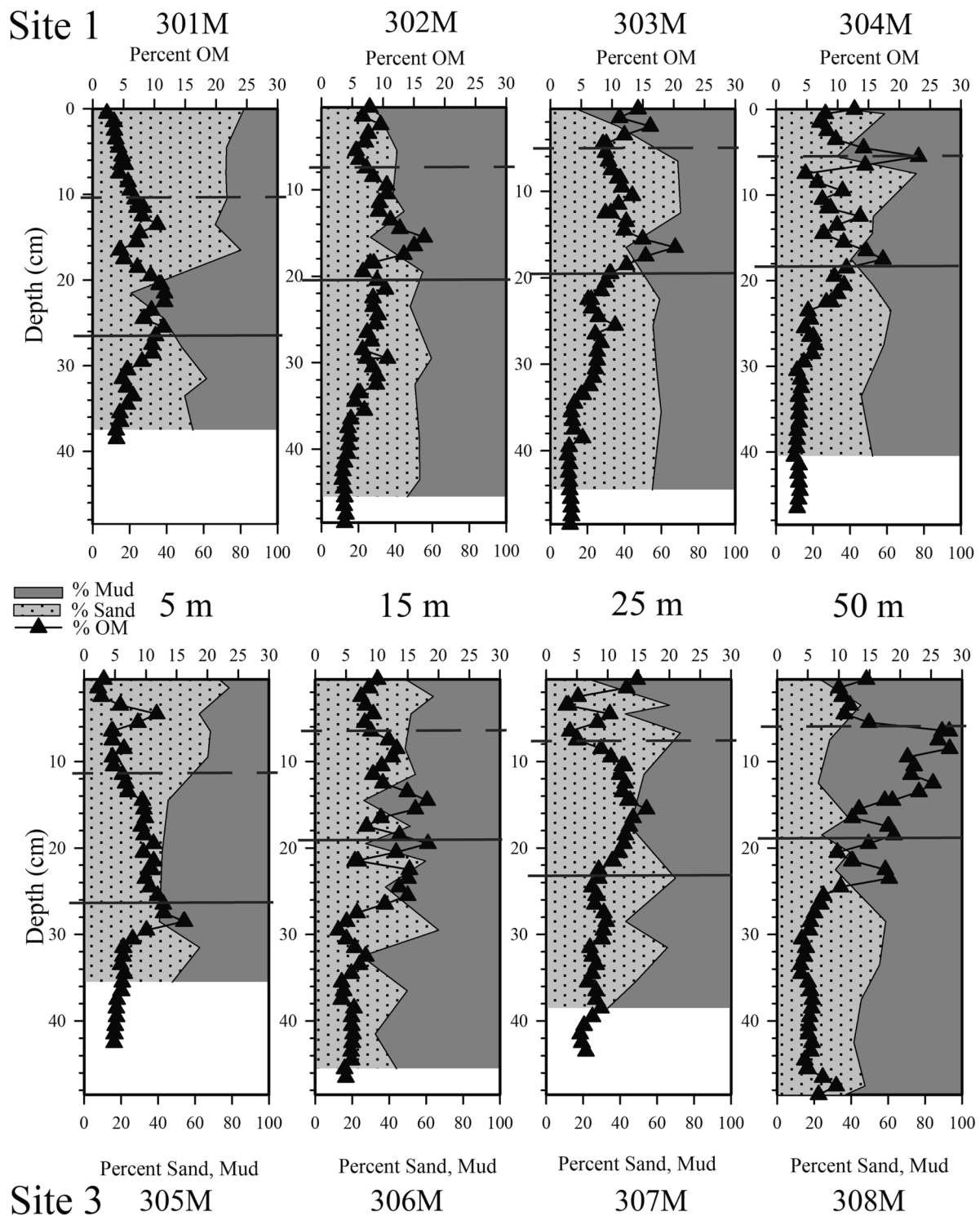
Fig. 2 Downcore ratio of percent sand (light gray dotted) and mud (silt + clay; solid dark gray; bottom axis) with percent organic matter (OM; top axis) for each core collected at Site 1 (top row) and Site 3 (bottom row). Core profiles are arranged in increasing distance from the shore-line from left to right. Based on results from the constant rate of supply (CRS) model, the dashed horizontal line on each graph indicates ~2000 and the solid horizontal line indicates ~1950 age-depth
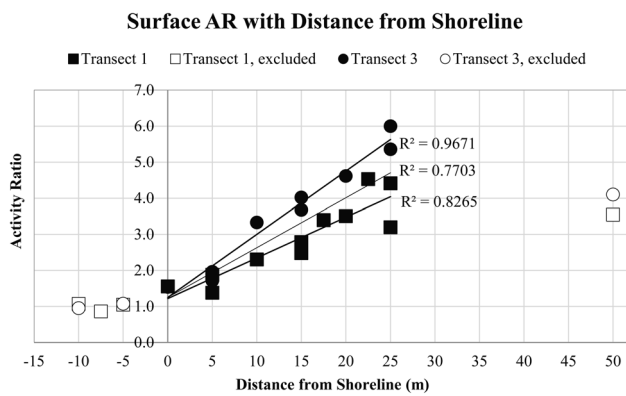
Fig. 3 Surficial and core top activity ratios (AR) of ^{210}Pb to ^{226}Ra from surface and marsh Site 1 transect 1 (squares) and surface and marsh Site 3 transect (circles) with 0 and the black vertical line representing the shoreline. Distance from the shoreline, in meters, is represented by positive and negative (−) numbers with negative indicating distance from shoreline into the estuary and positive numbers representing distance from the shoreline into the marsh. Solid black symbols represent samples used in calculation of regression (0–25-m distance from shoreline) while white symbols represent sample values excluded from the regression (50 m and estuarine samples). The dotted regression line ($R^2 = 0.9671$) is based on Site 3 AR data while the dashed regression line ($R^2 = 0.8265$) is based on Site 1 ARs. The solid black regression line ($R^2 = 0.7703$) encompasses all ARs, excluding those identified with white symbols

profiles of total and excess ^{210}Pb at sites further from the shoreline showed activity decreasing with depth but the profiles were not monotonic and varied in form between linear and exponential. Activity profiles for 303 M and 304 M contained zones with ^{210}Pb$_{xs}$ activities lower than stratigraphically deeper sediment; these zones occurred in sediment with DBD and OM that were slightly above (~10%) and below (~5%), respectively, the core average (Figs. 2 and 4). The ^{210}Pb$_{xs}$ inventories were quantifiably similar (30.2 ± 4.5 dpm/cm^2) and within the reported range for the region (Smith et al. 2013; Marot et al. 2019; Ellis and Smith 2021). ^{137}Cs was present at depth in all cores with terminal values between 21 and 32 cm and mid-depth maximum values between 16 and 25 cm indicating the peak activity of 1963 was recorded in the sedimentary record (Fig. 4; Table 2).

Age-depth relationships and sedimentation rates are presented for the CRS model. Briefly, the CIC model was not selected due to the spatial variability of the marsh sediment AR which counters the assumption of a constant initial concentration. Similarly, the non-monotonic nature of the profiles counters the CFCS model assumptions; a comparison of the CFCS model with ^{137}Cs and the CRS results are available in the supplemental material (Table S3). Consistent depth integrated inventories support the assumption of a constant supply of ^{210}Pb$_{xs}$ to the sediment surface favoring the application of the CRS model. Furthermore, the CRS model predicted a standard error-bracketed of 1963 for the

^{137}Cs peak for five of the eight cores with a standard error range of 4.1–8.8 years. The outlier cores from Site 1 (302 M and 303 M) had predicted dates of 1950 ± 5.3 and 1944 ± 8.8 for the ^{137}Cs peak while the outlier from Site 3 (306 M) had a predicted date of 1954 ± 5.8 (Table 2). Even with the outliers, an expanded two standard error assessment results in cross-validation of all cores while retaining a mostly sub-decadal resolution. CRS model results were used to chronologically constrain sedimentological and biofacies shifts indicative of environmental change and are presented in four forms: (1) age-depths, LSR, and MAR derived for each analyzed core interval (Table S4); (2) average LSR and MAR for each core (Table 2); (3) decadal LSR and MAR averages using a 13-year window (Table 3); and (4) a centennial (100 years) average of LSR and MAR (Table 3). A comparison of CRS and the constant flux constant supply model results are available (Table S3).

Since the early 1900s, MARs spanned two orders of magnitude (0.29–13.25 kg/m^2/year) (Table S4). Decadally averaged MARs illustrate sediment accumulation variability through time over the last century (Table 3). In all cores, average MARs over the last two decades were greater than the centennial average and two to four times the MAR observed during the first half of the twentieth century (Table 3). Fastest accumulation rates occurred at the 5-m sites during the last decade (Table 3, Table S4). Average MARs from Site 1's high energy shoreline became nearly evenly paced with each other in the 1970–1980s while Site 3's average MARs exhibit more decadal variability and become evenly paced with each other in 1960–1970s. It was not until after the ~1980s that MARs show large deviations from one another (Table 3).

Foraminifera

A total of 24 foraminiferal species (taxonomic reference list in Ellis et al. 2021) were identified in the cores ($n = 69$). Only agglutinated taxa were found in abundance (> 0.5% of a single sample): 11 species comprised ≥ 5% abundance of at least one sample, 8 species were rare (occurred ≤ 5 times across all samples) and 6 species were considered dominant and exhibited a mean abundance ≥ 5% across all samples ($n = 69$): *A.* cf. *A. salsum* (8.5%), *Ar. mexicana* (49.0%), *H. wilberti* (6.3%), *M. fusca* (5.8%), *T. inflata* (9.5%), and *Ti. comprimata* (6.8%). Abundances of *A.* cf. *A. salsum* and *M. fusca* were highly correlated ($r = 0.80$) and anti-correlated with *Ar. mexicana* ($r = −0.69$ and $−0.71$, respectively; Table S5). Estuarine species *P. simplissima*, an indicator of estuarine sediment deposition, exhibited a moderate inverse relationship with *Ar. mexicana* ($r = −0.48$); no other dominant or characteristic species exhibited a correlative relationship > ± 0.38 (Table S5). Potential impacts to the data quality and interpretation due to agglutinated
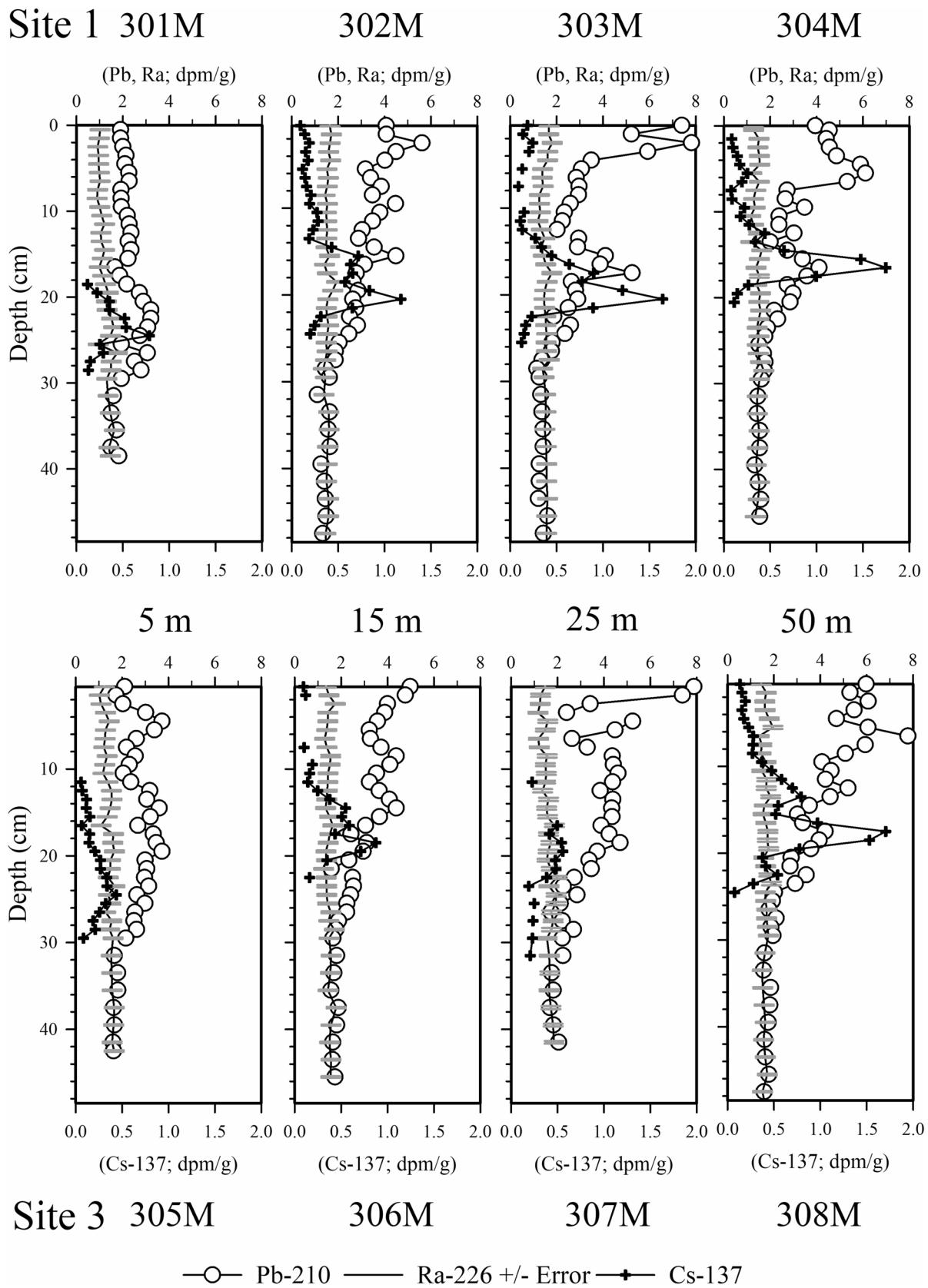
degradation were thoroughly explored via statistical analyses (Supplemental Methods, Table S6) and were determined to be less pronounced than the samples environmental signal.

Surficial Taxa, Distribution, and PCA Results

Surficial foraminifera and their environmental preferences in GB were assessed for the identification of the modern biofacies, to assess estuarine incursion, and for comparison with downcore assemblages. Core tops contained primarily *A.* cf. *A. salsum*, *Ar. mexicana*, and *M. fusca*, with abundances of *A.* cf. *A. salsum* and *M. fusca* anti-correlated with *Ar. mexicana* (Fig. S5). The PCA performed on the upper-most intervals for each core highlights this inverse association on Axis 1 with an eigenvalue of 0.5517 (Fig. 5; Table 4). On the biplot, *Ar. mexicana* loosely aligns with common middle marsh, high marsh, and upland transition species and increased d50 and opposite of *A.* cf. *A. salsum* and *M. fusca*, which loosely plot with increased percent OM (Fig. 5). Regarding distribution, the middle marsh, high marsh, and upland transition species, *T. inflata*, *Ti. comprimata*, and *H. wilberti*, respectively, were more abundant at Site 3 than Site 1 and most abundant in the 5- and 50-m core tops (301 M, 305 M and 304 M, 308 M, respectively). *P. simplissima* was abundant in core tops at 5 m from the shoreline with abundance decreasing with increased distance from the shoreline. The PCA exhibited the same relationship with *P. simplissima,* plotting opposite of distance from the shoreline and closely aligned with elevation, which decreases with distance from the shoreline, along Axis 2 with an eigenvalue of 0.3298 (Fig. 5; Table 4).

Downcore Cluster and Non-Parametric Analyses

The hierarchical cluster analysis, with a cophenetic correlation of 0.69, used to identify downcore assemblages, resulted in five cluster groups; three cluster groups contained 65/69 of the samples (Figs. 6 and 7). Due to the numerous shared species in each cluster group (i.e., relative low diversity; Table 5), the similarity among the groups was high with primary branching occurring between 57.8 and 68.5% similarity (Fig. 7). Marsh cluster group-1 (MC-1) was the only cluster group dominated by low marsh species (*A.* cf. *A. salsum, M* = 35.4%; *M. fusca, M* = 17.1%) with middle marsh species *Ar. mexicana* (*M* = 19.0%; Table 5; Goldstein

and Watkins 1999; Edwards and Wright 2015; Haller et al. 2019). The abundance of *P. simplissima*, an invasive estuarine species that has not been found living in the marsh (Ellis and Smith 2020, 2021; Haller et al. 2018, 2019; Osterman and Smith 2012) in MC-1 is notable (Table 5). MC-1 had the highest average density, with 9/10 samples from Site 1, and 8/10 samples from < 10 cm depth (Fig. 8; Table 5; Table S4). In comparison, MC-2 contains low marsh species (*A.* cf. *A. salsum*, *M. fusca*,) but in pointedly lower abundance than MC-1 along with an increased abundance of middle marsh (*Ar. mexicana*, *M* = 36.7%; *T. inflata*, *M* = 11.1%; *Ti. comprimata*, *M* = 5.9%) and upland and/or high salinity species (*H. wilberti*; Table 5; Kemp et al. 2009; Haller et al. 2019; Culver and Horton 2005). The abundance of *P. simplissima* in MC-2 was nearly equivalent (*M* = 9.1%; Table 5; Fig. 7) to MC-1. MC-2 was comprised of intervals from all cores except 308 M (*n* = 16) and had the highest average diversity (Fig. 8; Table 5, S4). MC-3, the largest cluster group (*n* = 39), had the lowest average density, and was heavily *Ar. mexicana* dominant (*M* = 63.4%) with only *T. inflata*, *Ti. comprimata*, and *H. wilberti* as subsidiary species (Fig. 7; Table 5). Low marsh and estuarine species are nearly absent in MC-3, making it the most comparable to the middle marsh assemblages in Haller et al. (2019). While 33/39 samples occurred at > 10-cm depth, the MC-3 cluster also included 308 M core top (Fig. 8; Table S4). MC-4, comprised of only a single sample (306 M 40–41 cm), was *Ar. mexicana* monospecific (90.5%) and will not be discussed further (Figs. 6, 7, and 8; Table 5). MC-5, made up of three samples from Site 3 was very dissimilar from all other clusters. It is distinguished by the dominance of *H. wilberti* (*M* = 55.0%) with only *Ar. mexicana* (*M* = 22.4%) and *T. inflata* (*M* = 12.9%) averaging > 4%; *H. wilberti* occurred in only small amounts (M ≤ 6.0%) in all other cluster groups (Table 5). Within 25 m of the modern shoreline, there is a shift both laterally and vertically from MC-3 to MC-2 and MC-1 (Fig. 8). The decrease in elevation from the shoreline to 50 m (Site 1) and 25-m (Site 3), due to the presence of a berm, results in "thick" transitional biofacies units (MC-1, MC-2) close to the shoreline that "pinch-out" with distance from the shoreline (Fig. 8).

All the clusters in this study contain species that dominated the middle marsh biofacies in Haller et al. (2019; *Ar. mexicana*, *Ti. comprimata*, *T. inflata*; Table 1). The low elevation gradient at Sites 1 and 3 (9.7 and 8.1 cm, respectively; Fig. 1), compared to other coastal marsh foraminifera studies where large environmental gradients were sampled (e.g., Kemp et al. 2009; Haller et al. 2019), cause the relative abundances of shared species and the presence of environmental indicator species to drive the dissimilarity among the biofacies (Table 5; Fig. 7). While a middle marsh interpretation is consistent with the marsh vegetation, foraminiferal data allow additional refinement of the middle marsh. We

Table 2 Constant rate of supply (CRS) model results for core sediment mass accumulation rates (MAR; in kilograms per square meter per year, kg/m²/y) and linear sedimentation rates (LSR; in centimeters per year, cm/y) with the respective standard deviation (Std Dev) at each site. The depth intervals (in centimeters, cm) used in the calculation for the development of the respective MAR and LSR model rates are provided. The maximum ^{137}Cs activity level in each core is provided as both the 1-cm midpoint depth and the calculated mass depth (in grams per square centimeter, g/cm²) for each core. The maximum ^{137}Cs activity level with its corresponding error in disintegrations per minute per gram (dpm/g) is provided along with the corresponding age-depth as determined using the CRS model, in years (y). Cores at each site are ordered from closest (5 m) to furthest (50 m) from the shoreline

	Site 1				Site 3			
Distance from Shoreline (m)	**5**	**15**	**25**	**50**	**5**	**15**	**25**	**50**
Core ID	**301 M**	**302 M**	**303 M**	**304 M**	**305 M**	**306 M**	**307 M**	**308 M**
Model depth intervals (cm)	0–30	0–28	0–26	0–25	0–34	0–28	0–32	0–28
Mean MAR ± Std Dev (kg/ m²/y ± kg/ m²/y)	3.93 ± 0.87	1.70 ± 0.43	1.81 ± 0.59	1.54 ± 0.37	3.86 ± 1.09	1.59 ± 0.38	2.47 ± 1.25	1.03 ± 0.44
Mean LSR ± Std Dev (cm/y ± cm/y)	0.567 ± 0.127	0.345 ± 0.098	0.309 ± 0.060	0.344 ± 0.151	0.592 ± 0.189	0.320 ± 0.069	0.406 ± 0.053	0.314 ± 0.096
^{137}Cs **Maximum; Midpoint depth (cm)**	24.5	20.5	20.5	16.5	24.5	18.5	19.5	17.5
^{137}Cs **maximum; mass depth (g/ cm²)**	21.4	13	11.6	9.6	19.3	11.6	12	7.2
^{137}Cs **activity ± error (dpm/g ± dpm/g)**	0.78 ± 0.07	1.17 ± 0.09	1.64 ± 0.08	1.75 ± 0.11	0.44 ± 0.05	0.87 ± 0.09	0.56 ± 0.15	1.71 ± 0.16
^{137}Cs **peak year ± Std. Dev. (y)**	1961 ± 4.5	1950 ± 5.3	1944 ± 8.8	1965 ± 4.1	1961 ± 4.8	1954 ± 5.8	1965 ± 6.6	1959 ± 7.4

propose the following environmental interpretations and biofacies based on the foraminiferal assemblages:

MC-1.   mixed low-to-middle marsh with estuarine deposition,
MC-2.   middle marsh with estuarine deposition,
MC-3.   middle marsh, and
MC-4.   upland deposition in middle marsh (Fig. 8).

The designation of estuarine deposition in MC-1 and MC-2 indicates allochthonous deposition due to the presence of estuarine *P. simplissima* in contrast to units containing species that are exclusively or dominantly autochthonous in low or middle marsh environments. Similarly, the designation of upland deposition in MC-5 indicates allochthonous deposition due to the abundance of *H. wilberti* and presence of *S. lobata*. The ANOSIM found both core distance from the shoreline ($r = 0.355$, $p = 0.001$) and core depth ($r = 0.487$, $p = 0.001$) were important regarding downcore foraminiferal distribution while site location (1, 3) was not ($r = 0.196$, $p = 0.017$; Fig. S6; Table S7). The NMDS

produced a moderate 2D stress value of 0.14 and 3D stress value of 0.1 and showed core intervals arranged from the top left to bottom right with increasing distance from the shoreline (Fig. 6; Fig. S7). Cluster group identifiers overlain on the NMDS indicate data arrangement trends across different statistical methods are consistent (Fig. 6).

Shoreline-Change Rates

Shoreline change rates at both sites increased over time. The average modern (2016–2017) shoreline-change rates of -0.95 ± 0.18 at high energy Site 1 and -0.88 ± 0.28 m/ year at protected Site 3 were 2.8 times greater than the average short-term (1957–2017) shoreline-change rates and 3.6 times and 5.7 times greater than the average long-term (1848–2017) shoreline change rate at Sites 1 and 3, respectively (Table 6). Modern and short-term shoreline change rates were greater at Site 1 than Site 3, but long-term rates were slightly lower (-0.17 ± 0.01 m/year versus -0.24 ± 0.01 m/year; Table 6).

Table 3 Decadally averaged sediment mass accumulation rates with associated errors, in kilograms per square meter per year (kg/m²/y), as determined by the constant rate of supply (CRS) model for all sites and distances Age-depths utilized for decadal averages are for 13-year windows (i.e., 10 ± 1.5 y, therefore the corresponding age-depths utilized for 1990–2000 are 1988.5–2001.5) are available in Table S4. ND indicates no data for the specified time frame. Cores are arranged in increasing distance from the shoreline from left to right

Distance from Shoreline (m)	Site 1				Site 3			
	5	15	25	50	5	15	25	50
Core ID	301 M	302 M	303 M	304 M	305 M	306 M	307 M	308 M
Decadally Averaged Mass Accumulation Rates (kg/m²/y)								
2010–present	7.81 ± 1.58	2.96 ± 0.43	1.67 ± 0.19	2.54 ± 0.29	7.79 ± 1.63	2.80 ± 0.33	4.14 ± 0.74	1.91 ± 0.21
2000–2010	5.63 ± 1.15	3.05 ± 0.52	2.15 ± 0.40	1.58 ± 0.19	5.60 ± 1.09	3.11 ± 0.49	4.61 ± 0.88	1.68 ± 0.24
1990–2000	3.98 ± 0.83	2.28 ± 0.36	2.75 ± 0.72	1.96 ± 0.32	3.33 ± 0.60	2.13 ± 0.35	2.46 ± 0.44	0.92 ± 0.13
1980–1990	3.80 ± 1.03	1.70 ± 0.34	2.82 ± 1.08	2.17 ± 0.56	2.10 ± 0.40	1.72 ± 0.32	1.73 ± 0.39	1.10 ± 0.23
1970–1980	1.60 ± 0.35	1.51 ± 0.38	1.61 ± 0.27	1.90 ± 0.57	1.61 ± 0.34	1.05 ± 0.19	1.36 ± 0.33	1.03 ± 0.27
1960–1970	1.24 ± 0.28	1.37 ± 0.54	1.25 ± 0.16	0.77 ± 0.20	1.41 ± 0.35	1.30 ± 0.41	1.12 ± 0.32	0.99 ± 0.31
1950–1960	1.16 ± 0.31	1.53 ± 0.75	1.07 ± 0.43	0.74 ± 0.24	1.16 ± 0.32	1.26 ± 0.44	1.79 ± 0.88	0.57 ± 0.20
1935–1950	0.79 ± 0.27	0.89 ± 0.39	0.63 ± 0.31	0.61 ± 0.23	1.15 ± 0.47	1.21 ± 0.67	2.76 ± 4.03	0.61 ± 0.30
pre-1935	0.69 ± 0.28	0.44 ± 0.25	0.81 ± 0.68	0.61 ± 0.35	4.78 ± 0.82	0.51 ± 0.26	ND	0.44 ± 0.26
Averaged Centennial Mass Accumulation Rates (kg/m²/y) per Site/Distance								
Mean	2.97	1.75	1.64	1.43	3.21	1.68	2.50	1.03
Std. Dev.	± 2.51	± 0.88	± 0.80	± 0.76	± 2.36	± 0.85	± 1.28	± 0.49

Discussion

Lithologic and foraminiferal data from two sites were used to distinguish depositional biofacies within the shallow marsh sediments. When paired with site-specific sediment accumulation rates (e.g., LSR, MAR) that account for variations in sedimentology (e.g., DBD, OM, grain-size) and shoreline change rates, we can assess short- and long-term sediment depositional and erosional trends and calculate distance from the shoreline downcore (Table S4). Terrano (2018) and Smith et al. (2021a) showed that at Sites 1 and 3, shorelines have been eroding for the past 100 years or more, meaning
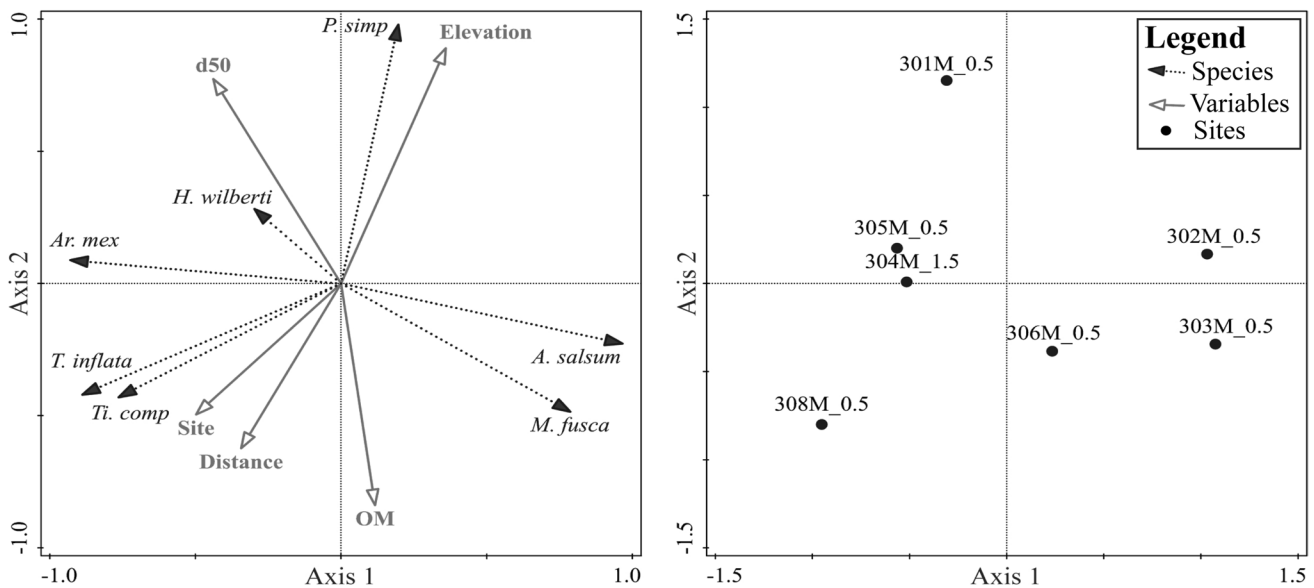

Fig. 5 Results of the non-parametric principal component analysis (PCA) on the six most dominant species (*Ar. mex = Arenoparella mexicana*; *Ti comp = Tiphotrocha comprimata*) and *Paratrochammina. simplissima* (*P. simp*), a dominant estuarine foraminifer in Grand Bay (Ellis and Smith 2021) indicated in black with dotted lines, with sedimentological parameters median grain-size (d50) and organic matter (OM) content, and site information including elevation, which generally decreases away from the shoreline with distance, the site location on the east or west side of Middle Bay, and distance from shoreline at Sites 1 and 3 (5, 15, 25, and 50 m), all indicated in gray with solid lines. Species abbreviations utilized in the figure are available in Table S2

Table 4 Summary of principal component analysis (PCA) on square root transformed core top foraminiferal abundance data with supplementary variables. Total variation is 84.7378, supplementary variables account for 95.6%, adjusted explained variation is 73.6%

Summary table

	Axis 1	Axis 2	Axis 3	Axis 4
Eigenvalues	0.5517	0.3289	0.0635	0.0465
Explained variation (cumulative)	55.17	88.05	94.4	99.05
Pseudo-canonical correlation (suppl.)	0.9945	1	0.6551	1

modern observational points are closer to the shoreline than in the past. Similarly, Smith et al. (2021a) calculated that mass of sediment exhumed from the shoreline due to erosion is nearly balanced by sediment deposited within 25 m of the shoreline. Therefore, the geometry, vertical, and lateral position of depositional (bio)facies are dependent on both the shoreline position through time and net sediment transport patterns, which are controlled by sediment supply and hydrodynamic energy (waves, currents, tides). Together, shoreline change rates, sedimentologic trends, geochronologic models and marsh biofacies (Fig. 8; Table S4) can be used to identify and chronologically constrain the marsh's environmental evolution over the past century and better understand marsh
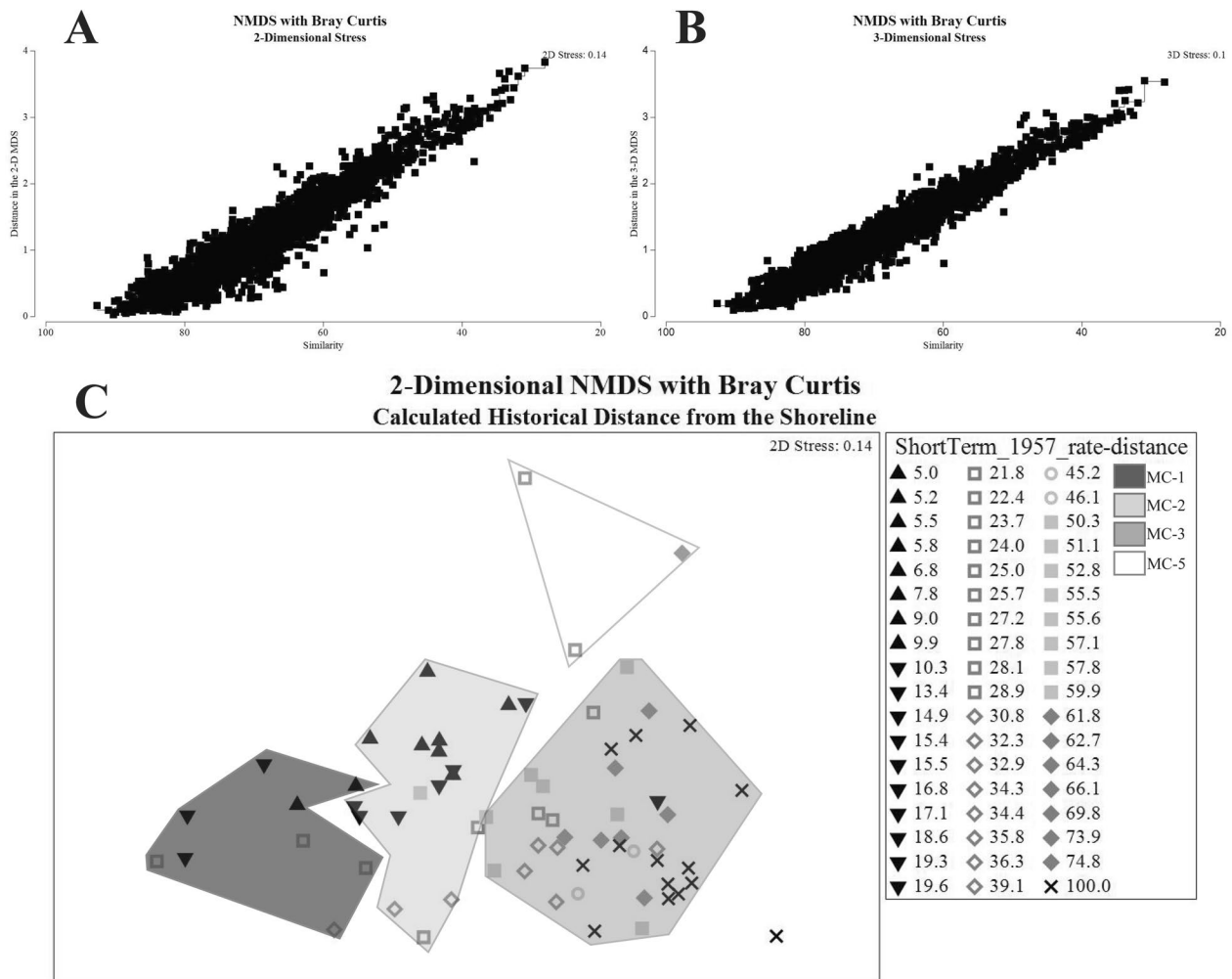
Fig. 6 Non-metric multi-dimensional scaling (NMDS) plots developed in Primer7 using the Kruskal stress formula on square root transformed abundance data with a Bray-Curtis similarity index. **A** and **B** show 2D and 3D similarity plots with stress values of 0.14 and 0.1, respectively; **C** 2-dimensional NMDS results with each foraminiferal sample core interval represented. Each sample is symbolized with the interval's calculated historic distance from the shoreline based on (1) the short-term shoreline change rate from 1957 to 2017 of −0.34 and −0.31 for Sites 1 and 3, respectively, and (2) the modern distance from the shoreline. Values of 100 indicate samples older than the 100-year age-depth confidence threshold. Biofacies groups MC-1 through MC-5 are indicated with polygons over each sample included in each biofacies; the single sample not included inside of a polygon was a monospecific sample that clustered alone (MC-4). Biofacies groups are defined as the following: MC-1: mixed low-to-middle marsh with estuarine deposition, MC-2: middle marsh with estuarine deposition, MC-3: middle marsh, and MC-5: upland deposition in middle marsh
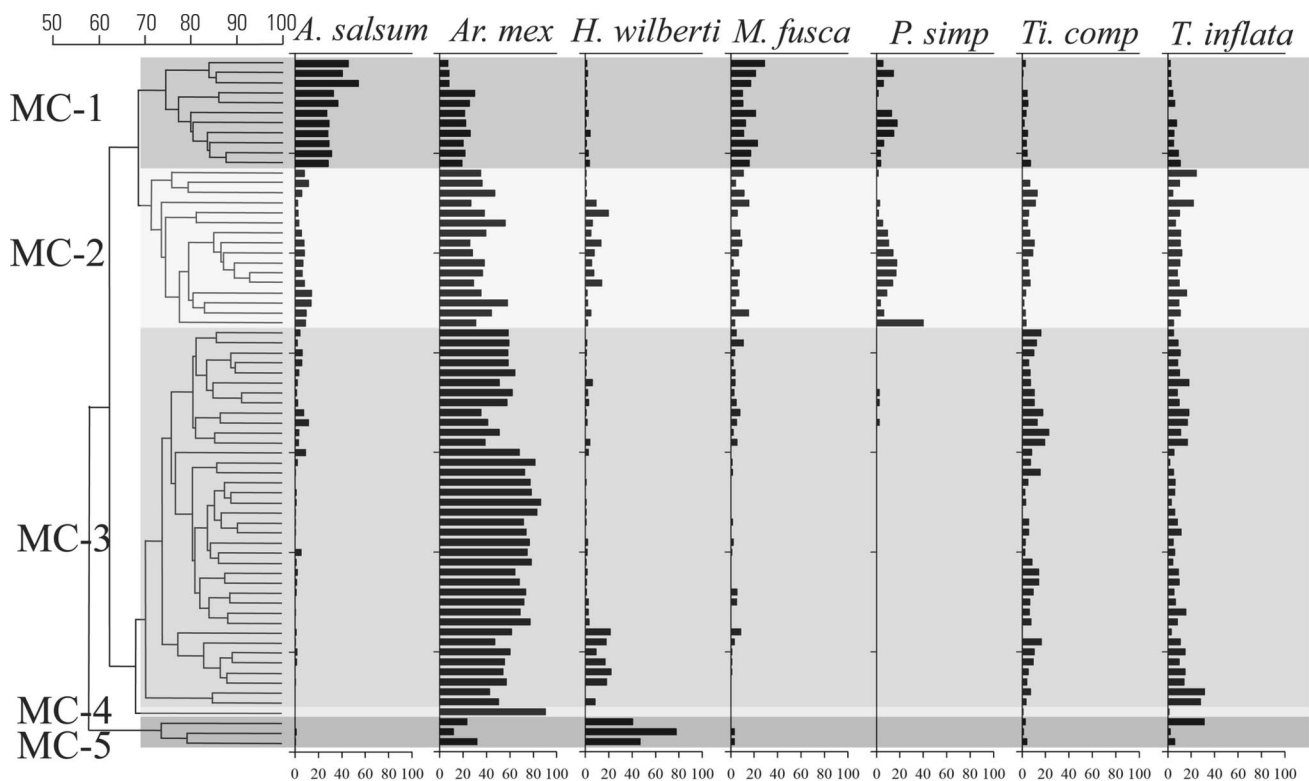
Fig. 7 Cluster analysis groups (MC-1, MC-2, MC-3, MC-4, and MC-5) based on a square-root transformation of all species abundance data, excluding unidentified calcareous, agglutinated, and organic lining specimens, with a Bray Curtis similarity index shown in the upper left corner. Six most dominant species and *Paratrochammina simplissima* (*P. simp*) abundances for each corresponding sample in the cluster analysis with each cluster group highlighted in a different shade of gray. Biofacies groups are defined as the following: MC-1: mixed low-to-middle marsh with estuarine deposition, MC-2: middle marsh with estuarine deposition, MC-3: middle marsh, and MC-5: upland deposition in middle marsh. Species abbreviations utilized in the figure are available in Table S2

response to shoreline erosion and increased inundation (i.e., event-driven, tides, and sea-level). Constraining the timing and response of shoreline proximal-marsh environments to changes in sediment availability, sediment provenance, and hydrodynamic energy is critical for managing the current ecosystem and projecting future changes.

Marsh Evolution Indicated by Foraminiferal Biofacies

Stratigraphic correlation of biofacies and sediment geochronologies outline the recent geologic evolution of these shore-proximal marshes. While the upper biofacies are different for each transect (MC-1 at Site 1; MC-2 at Site 3), the sedimentary records at both sites suggest synchronous deposition of estuarine-influenced sediment in the upper stratigraphic unit, which extends 15–25-m inland from the shoreline. At high-energy Site 1, the mixed low-to-middle marsh with estuarine deposition (MC-1) and middle marsh biofacies with estuarine deposition (MC-2) overlay the middle marsh biofacies (MC-3; Fig. 8) consistent with a marine transgression. The shift from middle marsh biofacies (MC-3) to the middle marsh with estuarine deposition biofacies (MC-2)

began around the 1960s and the mixed low-to-middle marsh biofacies with estuarine deposition (MC-1) has been actively replacing MC-2 at 5, 15, and 25 m from the shoreline since the early 2000s (Fig. 8; Table S4). From the early 1900s through the 1950s from ~35 m to > 80 m from the shoreline, middle marsh was prevalent at Site 1 (Table S4). Core 304 M, 50-m inland of the high-energy shoreline, is historically comprised of middle marsh biofacies throughout and contains the middle marsh with estuarine deposition biofacies at the core top (Fig. 8). Based on the marsh-type shifts seen along Site 1, the estuarine deposition 50-m inland is likely the result of an episodic event (e.g., storm) rather than fair weather conditions. We expect that the core top will return to middle marsh until the shoreline erodes enough for this 50-m site to exist within 25–35 m of the shoreline at which time a biofacies shift reflecting regular estuarine deposition would be expected around 2031 based on the modern shoreline change rate for the site. The marsh evolution evidenced by the biofacies shifts is in response to the transgressive nature of the GB marshes due to reduced protection from the submerged Grand Batture Island and consequently, increased lateral shoreline erosion (Table 6).

Table 5 Average species abundances, densities (N, per 1 ml), richness (S, per 1 ml), and Fisher's alpha (α) diversity values for the five biofacies as determined by the hierarchical cluster analysis on square root transformed abundance data with a Bray Curtis similarity index. Marsh clusters are identified as MC-1, MC-2, MC-3, MC-4, and MC-5 with biofacies descriptions. Species abbreviations utilized throughout the table are available in Table S2

	MC-1	MC-2	MC-3	MC-4	MC-5
	Low marsh transition with estuarine deposition	Middle marsh with estuarine deposition	Middle marsh	Monospecific *Ar. mexicana*	Upland deposition in middle marsh
A. cf. *A. salsum*	35.4	8.8	2.2	0.0	0.5
Ar. mexicana	19.0	36.7	63.4	90.5	22.4
E. macrescens	0.5	1.0	1.2	0.0	0.0
H. wilberti	1.7	6.0	4.0	0.0	55.0
M. fusca	17.1	7.7	2.4	0.0	2.0
P. simplissima	8.2	9.1	0.2	0.0	0.1
S. lobata	2.2	2.3	2.4	1.8	2.0
Ti. comprimata	3.0	5.9	8.6	0.9	2.5
T. inflata	4.3	11.1	10.1	0.9	12.9
Density (N)	188	113	73	117	145
Richness (S)	14	14	10	6	9
Diversity (Fisher's α)	2.1	2.2	1.8	0.9	1.3

The mixed low-to-middle marsh biofacies with estuarine deposition, expansive at Site 1, is largely absent from Site 3 (Fig. 8). While both sites are regularly inundated by tides which provide estuarine deposition resulting in the presence of *P. simplissima*, the reduction of fetch and wind-waves due to the more protected location of Site 3, as indicated by the less erosive shoreline change rate compared with Site 1, has permitted proportionally greater abundances of middle marsh species to thrive within 15 m of the shoreline compared with Site 1. Overall, a similar but delayed and less temporally and laterally constrained transition is evident at Site 3 as Site 1 with the modern middle marsh with estuarine deposition extending inland ~19 m from the shoreline and back to at least the early 2000s (Table S4) while the middle marsh biofacies is dominant > 22 m from the shoreline.

Environmental Response to a Progressively More Exposed Estuary Following the Submergence of Grand Batture Island

The submergence of Grand Batture Island following Hurricanes Camille (1969) and Frederic (1979) and the subsequent hydrologic changes and shift in sediment supply are evidenced in the coarsening upwards sequences found throughout GB estuary due to the increased availability of sandy sediments and loss of fine-grained sediments through ebb dominance (Ellis and Smith 2021). Due to the observed sediment feedback loops between the marsh and estuary and regular estuarine incursion within 25 m of the shoreline during fair-weather conditions, some of the estuarine trends associated with Grand Batture Island are also evidenced in the 5-m marsh cores. Additionally,

sediment depositional signatures in marshes due to hurricanes can vary for a variety of reasons including but not limited to estuarine sediment type, marsh and upland sediment type, ebb or flood tides, wave heights, extent of inland flooding, and distance from the shoreline (Lui and Fearn 1993; Hawkes and Horton 2012; Yao et al. 2018). Smith et al. (2021a) examined marsh sediment deposits in GB from Hurricane Nate (2017) and found that those deposited along the high energy shorelines had greater DBD (e.g., increased sand content) and less OM than sediments deposited during fair weather conditions (Smith et al. 2021a), while those deposited along the low energy, protected shorelines had similar physical properties to fair weather seasonal sediment deposition indicating different sediment sources.

The large sedimentological shift at ~21.5–17.5 cm depth in the 5-m core at Site 1 (Fig. 2) temporally corresponds with ~1975–1988 (Table S4), bracketing Hurricane Frederic; the subsequent sandy coarsening upwards sequence in the top 15 cm follows the complete submergence of Grand Batture Island. This time-period is also depicted by the CRS model as a period of rapidly increasing MAR from 1.3 to 5.3 kg/m²/year (Table S4). Based on the short-term shoreline-change rate, the marsh surface around 1975–1988 would have been approximately 14.9–19.3 m from the shoreline, within the expected shoreline range to receive fair weather estuarine sediment deposition (Lacy et al. 2020). These sedimentological and accumulation trends also correspond with the vertical biofacies change from a middle marsh to the low-to-middle marsh transitional biofacies B with estuarine deposition that currently extends 25 m from the shoreline (Fig. 8; Table S4). Together, these findings show that the

Fig. 8 Fence diagram of the four primary foraminiferal biofacies identified as MC-1, MC-2, MC-3, and MC-5 and defined as follows: MC-1 (vertical black bars behind dark gray)–mixed low-to-middle marsh with estuarine deposition; MC-2 (black dots behind light gray)–middle marsh with estuarine deposition; MC-3 (solid dark gray behind medium gray)–middle marsh; MC-5 (diagonal stippling behind white)–upland deposition in middle marsh. Core profiles are arranged with increasing distance from the shoreline from left to right with the core top position scaled vertically to account for changes in elevation; figure not scaled horizontally. Core tops represent 2016, the year collected, and based on results from the constant rate of supply (CRS) model, a black isochron line across Sites 1 and 3 represents approximately 2000 and 1950
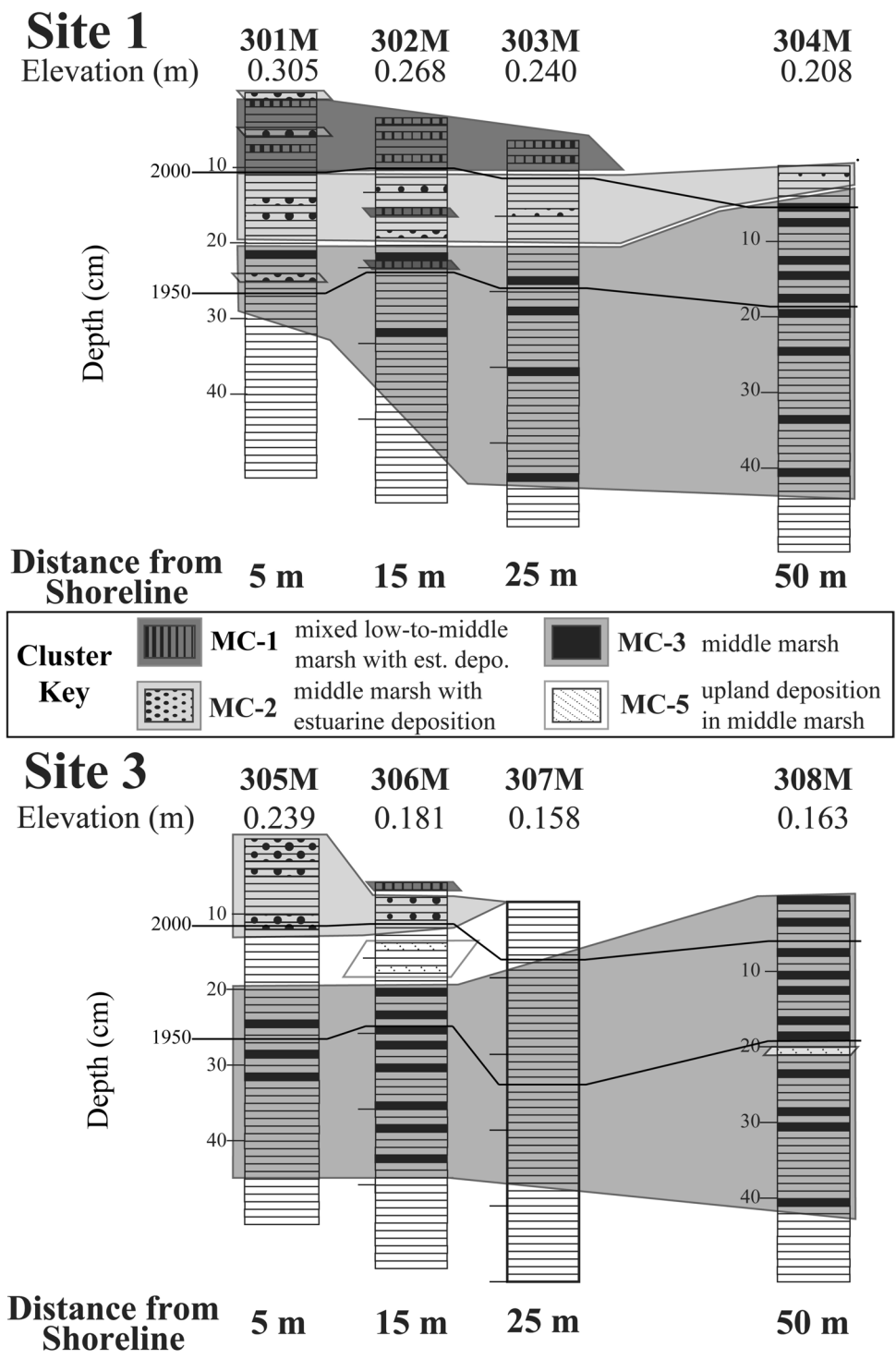
submergence of the sandy Grand Batture Island likely contributed to increased shoreline erosion, increased deposition of sandy sediments onto the marsh within 20 m of the shoreline and increased estuarine inundation that resulted in the environmental shift from middle marsh to middle marsh with estuarine deposition on to the modern a mixed low-to-middle marsh with estuarine deposition.

The 5-m core at Site 3 on the protected, low energy shoreline also experienced the environmental shift documented at Site 1 from middle marsh to the middle marsh with estuarine deposition biofacies downcore (11–25 cm), though dating is poorly constrained and occurred between ~1961 and 2000 (Table S4). However, since the initial jump in sediment MAR between ~1998 and 2001 (10–13 cm) from 3.4 to 7.1 kg/m²/

Table 6 Average shoreline-change rates, in meters per year (m/y), for each transect site (1, 3) and time period (modern, short-term, long-term), with the respective standard deviations (Std. Dev.)

	Shoreline-change rates (m/y)					
Site ID	Modern		Short-term		Long-term	
	Oct. 2016–Oct. 2017		1957–2017		1848–2017	
	Mean	Std. Dev. ($\pm$)	Mean	Std. Dev. ($\pm$)	Mean	Std. Dev. ($\pm$)
1	−0.95	0.18	−0.34	0.09	−0.17	0.01
3	−0.88	0.28	−0.31	0.01	−0.24	0.01

year and corresponding shift in grain-size from silt to sand, MAR increased over time and are the highest recorded among all cores (Table S4). From annual measurements, Smith et al. (2021a) reported 1.6 times more sediment was deposited than eroded at Site 1 and an equal proportion of erosion and deposition occurred at Site 3; unlike this study, it did not address the lateral change in distance from the shoreline in response to the eroding shoreline through time. The difference in approach is likely the reason for Site 3 exhibiting higher MAR and LSR than Site 1 despite its more protected location. Aside from the rapidly accelerating MAR observed in the cores closest to the shoreline, no other cores have temporally constrained sedimentological or biofacies shifts that can be directly attributed to the degradation of Grand Batture Island.

At both Sites 1 and 3, estuarine *P. simplissima* was identified at 50 m from the shoreline, beyond the fair-weather distance (25 m) where estuarine sediments are routinely deposited (Smith et al. 2021a). At high energy Site 1, the presence of estuarine and low marsh foraminifera at 1–2 cm depth resulted in a biofacies alteration (Fig. 8) that coincided with a near doubling in MAR (Table S4), an increase in percent sand, and decrease in OM content (Fig. 2) around ~2014. Similarly, at low energy shoreline Site 3, *P. simplissima* was preserved at 3–4 cm depth though its presence did not result in a biofacies shift. The sediments and OM content associated with the 3–4 cm were also coarser and less organic than those below (Fig. 2) and corresponded with ~2008. Given the distance from the shoreline and estuarine signature of these deposits, it is likely that both correspond to storm events or extreme high tide or flood events.

Fifteen meters inland of the low energy shoreline, a unit identified as upland deposition in middle marsh (MC-5) was identified in a very coarse silt deposit at 8–12 cm depth, corresponding to ~1985–1995 and at a historical distance ~22–25 m from the shoreline (Fig. 8; Table S4). This deposit corresponds with an increase in percent sand and decrease in OM (relative to 14–15 cm) and retains an OM content comparable to upland and low and middle marsh environments (Haller et al. 2019). Given the approximate deposition date, it is possible the biofacies is the result of an upland debris deposit or preserved wrack line, initially deposited during Hurricane Elena (1985), which caused 2.4 m tides

in Pascagoula, MS. Because the top 33 cm of the 15-m core contains five sedimentological shifts with a > 25% change in percent sand/mud over ≤ 5 cm (Fig. 2), the ability to differentiate between other event-driven deposits and fair-weather deposits is difficult. Despite the sedimentologic shifts and because all intervals below 12 cm are identified as middle marsh, do not contain *P. simplissima*, and short-term shoreline change rates have the site located > 25 m from the shoreline (Table S4), it is likely the sediment between 12 and 20 cm (~1985–1948) is from reworked marsh or upland sediments rather than the estuary.

Evidence of Estuarine and Marsh-Edge Sediment Re-working and Re-deposition

The fining-inland sedimentological pattern observed at both sites, along with the increase in OM with distance from the shoreline within 25-m of the shoreline (Fig. S3A, C), is consistent with patterns of allochthonous sediment transport and delivery into the marsh from adjacent water bodies in other studies (Stumpf 1983; Duvall et al. 2019). Smith et al. (2021a) and Lacy et al. (2020) found calm-weather estuarine conditions limit landward deposition with 60–90% of sediment mass deposited within 10 m of the shoreline. Duvall et al. (2019) found that shoreline positioning relative to wind direction and subsequent maximum fetch was an important factor in controlling sediment deposition in microtidal systems due to the ability of wind-driven waves and currents to elevate suspended sediment concentrations (SSC) over tidal flats. In GB, Nowacki and Ganju (2020) showed increased SSC along the northern and northwestern perimeter of Middle Bay, near Site 1, where fetch is greatest. This increased SSC is a likely source of the fine-grained allochthonous sediment and OM deposited inland at Site 1. A similar trend has been observed along low energy, tidal creek shorelines where OM and fine sediment particles are more readily transported further into the marsh during flood events than denser sediments (e.g., quartz sand) resulting in decreasing sediment texture with distance (French and Spencer 1993; Reed et al. 1999).

Fine-grained and organic-rich sediments retain atmospheric deposition of $^{210}Pb_{xs}$ at a higher rate than sandier sediments (Dinsley et al. 2019), like those deposited near the

shoreline, diluting atmospheric deposition of $^{210}Pb_{xs}$ at the shoreline. The trend of reduced ARs near the shoreline relative to ARs at 25 m, where values begin to plateau (Fig. 3), suggests that allochthonous estuarine inputs are limited to 20–25 m from the shoreline. The increase in sand content up-core and in the core tops nearest the shoreline is comparable to estuarine sediment grain-size from the vicinity (Haller et al. 2018; Marot et al. 2019; Ellis and Smith 2021), likely a result of recycled marsh material being deposited at the shoreline (Fig. 2; Hopkinson et al. 2018). Further supporting an estuarine sediment source within 25 m of the shoreline is the increased abundance of *P. simplissima*, a recently invasive estuarine species to this area (Ellis and Smith 2021), on the marsh surface within approximately 25 m of the shoreline (Fig. S5) and at depth (> 2%) at historical distances up to 28.1 m from the shoreline based on the short-term shoreline change rates for each site (excluding the single occurrences at depth in the 50-m cores; Table S4). The occurrence of *P. simplissima* at depth reflects sustained allochthonous estuarine input since the 1980s at Site 1, following the submergence of Grand Batture Island, and at least the early 2000s at Site 3 (Table S4).

Delivery of organic and inorganic estuarine and exhumed marsh sediments to the marsh are critical components of marsh accretion influencing marsh resilience to sea level rise yet are poorly refined in geomorphic coastal marsh models. Using the HydroMEM model, Alizad et al. (2016) showed that seaward dipping elevation gradients, which control tidal prism, often resulted in declining sedimentation rates; however, spatially varying SSC was not tested. Recently, Coleman et al. (2022) acknowledged discrepancies between modeled predicted marsh vulnerability using meta-analysis of SSC and vertical accretion measurements. One conclusion of their study was on the role SSC inventory (i.e., SSC multiplied by tidal prism) played on reducing discrepancy between measurement-based assessments and model-based predictions of marsh vulnerability (Coleman et al. 2022). Our findings coupled with Smith et al. (2021a) on nearshore marsh gradients that decrease towards the marsh interior provide insight to processes that require additional consideration regarding models and observation validation as these processes influence geomorphic evolution and marsh vulnerability over long timescales.

Conclusions

Grand Bay marsh evolution over the past century can be observed via downcore biofacies alterations chronologically constrained using foraminifera microfossils. Location at the time of the transition, relative to the shoreline, was determined using historical linear regression rates. Two sites were compared, a high-energy site that is readily exposed to high fetch, wind-wave energy from the south and southeast (direction of strongest winds) and a second site that is located within a sub-bay and generally protected from long fetch, wind-driven waves. From the early 1900s through the 1950s from ~35 to > 80 m, middle marsh was prevalent at the high energy site. The shift from middle marsh biofacies to one with estuarine deposition began around the 1960s, coinciding with the complete submergence of Grand Batture Island. Middle marsh biofacies with estuarine deposition were actively replaced by mixed low-to-middle marsh biofacies with estuarine deposition up to 25 m from the shoreline in the early 2000s. At the protected site, a similar transition is evident with the modern middle marsh biofacies with estuarine deposition extending inland ~19 m from the shoreline during the early 2000s. While the mixed low-to-middle marsh biofacies was expansive at the high energy site, it is largely absent from the low energy site, and middle marsh biofacies are still dominant a distances greater than 20 m from the shoreline.

The steady increase in percent clay and AR from the shoreline to 25-m inland followed by a decrease in both indicates that, in agreement with other studies, fair-weather estuarine deposition is limited to 25-m inland from the shoreline. However, estuarine and low marsh foraminifera species were preserved at 50 m from the shoreline, coincident with a large increase in MAR and sand, indicating storm deposition 50-m inland at both sites. However, due to the more protected nature of Site 3's shoreline, the sedimentological shift was reduced, and the microfossil shift did not result in a biofacies change like at Site 1. When sedimentological shifts are not apparent, the use of *P. simplissima* as an estuarine indicator for storm deposits in GB marsh sediments is valuable due to the dissolution of calcareous species in both the marsh and estuary. In response to the degradation of Grand Batture Island, marsh cores collected nearest the shoreline exhibit sandy coarsening upwards sequences and rapidly increasing MAR. The level of protection each shoreline historically received had a large influence on when sedimentological and MAR changes occurred. These data demonstrate that foraminiferal biofacies alterations capture marsh transitions coincident with shoreline change rates and can provide a relative proxy of distance from shoreline, illustrating that microfossils can be used to estimate past shoreline change in regions with fewer historical shoreline data sources.

Declarations

References

Alizad, K., S.C. Hagen, J.T. Morris, P. Bacopoulos, M.V. Bilskie, J.F. Weishampel, and S.C. Medeiros. 2016. A coupled, two-dimensional hydrodynamic-marsh model with biological feedback. *Ecological Modelling* 327: 29–43. https://doi.org/10.1016/j.ecolmodel.2016.01.013

Allen, J., and K. Pye. 1992. Coastal saltmarshes: their nature and importance. In *Saltmarshes: Morphodynamics, conservation and engineering significance*. Cambridge: Cambridge University Press.

Appleby, P.G. 2001. Chronostratigraphic techniques in recent sediments. In *Tracking environmental change using lake sediments. Volume 1. Basin analysis, coring, and chronological techniques*, ed. W.M. Last and J.P. Smol, 171–203. Dordrecht, The Netherlands: Kluwer Academic Publishers.

Appleby, P.G., and F. Oldfield. 1978. The calculation of lead-210 dates assuming a constant rate of supply of unsupported ^{210}Pb to the sediment. *CATENA* 5: 1–8.

Armynot du Châtelet, É., V. Bout-Roumazeilles, A. Riboulleau, and A. Trentesaux. 2009. Sediment (grain size and clay mineralogy) and organic matter quality: control on living benthic foraminifera. *Revue De Micropaléontologie* 52: 75–84.

Belknap, D., and J. Kelley. 2021. Salt marsh distribution, vegetation, and evolution. In *Salt marshes: function, dynamics, and stresses*, ed. D. FitzGerald and Z. Hughes, 9–30. Cambridge: Cambridge University Press. https://doi.org/10.1017/9781316888933.003.

Berkeley, A., C.T. Perry, S.G. Smithers, B.P. Horton, and K.G. Taylor. 2007. A review of the ecological and taphonomic controls on foraminiferal assemblage development in intertidal environments. *Earth Science Reviews* 83: 205–230.

Berkeley, A., C.T. Perry, and S.G. Smithers. 2009. Taphonomic signatures and patterns of test degradation on tropical, intertidal benthic foraminifera. *Marine Micropaleontology* 73: 148–163.

Binford, M.W. 1990. Calculation and uncertainty analysis of ^{210}Pb dates for PIRLA project lake sediment cores. *Journal of Paleolimnology* 3: 253–267.

Blott, S.J., and K. Pye. 2001. GRADISTAT—A grain size distribution and statistics package for the analysis of unconsolidated sediments. *Earth Surface Processes and Landforms* 26: 1237–1248.

Burningham, H., and M. Fernandez-Nunez. 2020. Chapter 19- Shoreline change analysis. In *Sandy beach morphodynamics*, ed. D.W.T. Jackson and A.D. Short, 439–460. Elsevier.

Buster, N.A., and R.A. Morton. 2011. *Historical bathymetry and bathymetric change in the Mississippi-Alabama coastal region, 1847–2009*. U.S. Geological Survey Scientific Investigations Map 3154.

Callaway, J.C., R.D. DeLaune, and W.H. Patrick Jr. 1997. Sediment accretion rates from four coastal wetlands along the Gulf of Mexico. *Journal of Coastal Research* 13: 181–191.

Chmura, G.L., and E.C. Kosters. 1994. Storm deposition and Cs-137 accumulation in fine-grained marsh sediments of the Mississippi delta plain. *Estuarine, Coastal and Shelf Science* 39: 33–44.

Chmura, G.L., A. Coffey, and R. Crago. 2001. Variation in surface sediment deposition on salt marshes in the bay of Fundy. *Journal of Coastal Research* 17 (1): 221–227 http://www.jstor.org/stable/4300165.

Clarke, K.R., and R.N. Gorley. 2015. *PRIMER v7: user manual/tutorial*. United Kingdom: PRIMER-E Ltd.

Coleman, D.J., M. Schuerch, S. Temmerman, G. Guntenspergen, C.G. Smith, and M.L. Kirwan. 2022. Reconciling models and measurements of marsh vulnerability to sea level rise. *Limnology and Oceanography Letters* 7: 140–149. https://doi.org/10.1002/lol2.10230.

Corbett, D.R., and J.P. Walsh. 2015. ^{210}Lead and ^{137}Cesium. In *Handbook of sea-level research*, ed. I. Shennan, A.J. Long, and B.P. Horton, 361–372. Chichester, UK: John Wiley & Sons Ltd.

Crowell, M., S.P. Leatherman, and M. Buckley. 1991. Historical shoreline change: error analysis and mapping accuracy. *Journal of Coastal Research* 7: 839–852.

Culver, S.J., and B.P. Horton. 2005. Infaunal marsh foraminifera from the outer banks, North Carolina, U.S.A. *Journal of Foraminiferal Research* 35: 148–170.

Culver, S.J., H.J. Woo, G.F. Oertel, and M.A. Buzas. 1996. Foraminifera of coastal depositional environments, Virginia, U.S.A.; distribution and taphonomy. *Palaios* 11: 459–486.

Cutshall, N.H., and I.L. Larsen. 1986. Calibration of a portable intrinsic Ge gamma-ray detector using point sources and testing for field applications. *Health Physics* 51: 53–59.

Cutshall, N.H., I.L. Larsen, and C.R. Olsen. 1983. Direct analysis of 210Pb in sediment samples: self-absorption corrections. *Nuclear Instruments and Methods* 206: 309–312.

Davies, D.J., and R.L. Hummell. 1994. Lithofacies evolution from transgressive to highstand systems tracts, Holocene of the Alabama coastal zone. *Gulf Coast Association of Geological Societies Transactions* 44: 145–153.

De Rijk, S., and S. Troelstra. 1999. The application of a foraminiferal actuo-facies model to salt marsh cores. *Palaeogeography, Palaeoclimatology, Palaeoecology* 149: 59–66.

Dean, W.E. 1974. Determination of carbonate and organic matter in calcareous sediments and sedimentary rocks by loss on ignition—comparison with other methods. *SEPM Journal of Sedimentary Research* 44: 242–248.

Debenay, J.-P., E. Tsakiridis, R. Soulard, and H. Grossel. 2001. Factors determining the distribution of foraminiferal assemblages in Port Joinville Harbor (Ile d'Yeu, France): the influence of pollution. *Marine Micropaleontology* 43: 75–118.

DeLaune, R.D., J.H. Whitcomb, W.H. Patrick Jr., J.H. Pardue, and S.R. Pezeshki. 1989. Accretion and canal impacts in a rapidly subsiding wetland. I. Cs-137 and Pb-210 techniques. *Estuaries* 12: 247–259.

Dinsley, J.M., C.J.B. Gowing, and A.L. Marriott. 2019. *Natural and anthropogenic influences on atmospheric Pb-210 deposition and activity in sediments — a review*. British Geological Survey Internal Report OR/17/047.

Diz, P., G. Francés, S. Costas, C. Souto, and I. Alejo. 2004. Distribution of benthic foraminifera in coarse sediment, Ría de Vigo, NW Iberian margin. *Journal of Foraminiferal Research* 34: 258–275.

Dolan, R., M.S. Fenster, and S.J. Holme. 1991. Temporal analysis of shoreline recession and accretion. *Journal of Coastal Research* 7 (3): 723–744 http://www.jstor.org/stable/4297888.

Duvall, M.S., P.L. Wiberg, and M.L. Kirwan. 2019. Controls on sediment suspension, flux, and marsh deposition near a bay-marsh boundary. *Estuaries and Coasts* 42: 403–424.

Edwards, R.J., and A.J. Wright. 2015. Foraminifera. In *Handbook of sea-level research*, ed. I. Shennan, A.J. Long, and B.P. Horton, 191–217. Chichester, UK: John Wiley & Sons Ltd.

Eleuterius, C.K., and G.A. Criss. 1991. *Point aux Chenes: past, present, and future perspective of erosion*. Ocean Springs, Mississippi: Physical Oceanography Section Gulf Coast Research Laboratory.

Ellis, A.M., and C.G. Smith. 2020. *Benthic foraminiferal data from surface samples and sedimentary cores in the Grand Bay estuary, Mississippi and Alabama*. U.S. Geological Survey data release. https://doi.org/10.5066/P9YCK857.

Ellis, A.M., and C.G. Smith. 2021. Emerging dominance of Paratrochammina simplissima (Cushman and McCulloch) in the northern Gulf of Mexico following hydrologic and geomorphic changes. *Estuarine, Coastal, and Shelf Science* 255: 107312. https://doi.org/10.1016/j.ecss.2021.107312.

Ellis, A.M., J.A. Jacobs, K.E.L. Smith, I.D. Atchia, and C.G. Smith. 2021. *Sediment core microfossil data collected from the coastal marsh of Grand Bay National Estuarine Research Reserve, Mississippi, USA*. U.S. Geological Survey data release. https://doi.org/10.5066/F7X63K24.

Ellis, A.M., C.G. Smith, J. Vargas, and C. Everhart. 2022. *Sediment and radiochemical characteristics from a shore perpendicular estuarine and marsh transect in the Grand Bay National Estuarine Research Reserve, Mississippi*. U.S. Geological Survey data release. https://doi.org/10.5066/P9BLFW2G.

Fenster, M.S., R. Dolan, and R.A. Morton. 2001. Coastal storms and shoreline change: signal or noise? *Journal of Coastal Research* 17: 714–720.

French, J.R., and T. Spencer. 1993. Dynamics of sedimentation in a tide-dominated backbarrier salt marsh, Norfolk, UK. *Marine Geology* 110: 315–331.

Galle, O.K., and R.T. Runnels. 1960. Determination of CO_2 in carbonate rocks by controlled loss on ignition. *Journal of Sedimentary Petrology* 30 (4): 613–618.

Gazzier, C.A. 1977. *Holocene stratigraphy of the Bayou cumbest fluvial system: southeastern Mississippi*, vol. 72. University of Mississippi M.S. thesis.

Gehrels, W., and A. Kemp. 2021. Salt marsh sediments as recorders of holocene relative sea-level change. In *Salt marshes: function, dynamics, and stresses*, ed. D. FitzGerald and Z.

Hughes, 121–131, 225–256. Cambridge: Cambridge University Press, Vienna. https://doi.org/10.1017/9781316888933.011

Goldberg, E.D. 1963. Geochronology with Pb-210. In *Radioactive dating*. Vienna: International Atomic Energy Agency.

Goldstein, S.T., and G.T. Watkins. 1999. Taphonomy of salt marsh foraminifera: an example from coastal Georgia. *Palaeogeography, Palaeoclimatology, Palaeoecology* 149: 103–114.

Goldstein, S.T., G.T. Watkins, and R.M. Kuhn. 1995. Microhabitats of salt marsh foraminifera: St. Catherines Island, Georgia, USA. *Marine Micropaleontology* 26: 17–29.

Haller, C. 2018. *Application of modern foraminiferal assemblages to paleoenvironmental reconstruction: case studies from coastal and shelf environments*. Graduate Theses and Dissertations. https://scholarcommons.usf.edu/etd/7627. Accessed 1 Jun 2021.

Haller, C., C.G. Smith, T. McCloskey, M.E. Marot, A.M. Ellis, and C.S. Adams. 2018. *Benthic foraminiferal data from the Eastern Mississippi sound salt marshes and estuaries*. U.S. Geological Survey data release. https://doi.org/10.5066/F7MC8X5F.

Haller, C., C.G. Smith, P. Hallock, A.C. Hine, L.E. Osterman, and T. McCloskey. 2019. Distribution of modern salt marsh foraminifera from the eastern Mississippi Sound, U.S.A. *Journal of Foraminiferal Research* 49: 29–47.

Hammer, ∅, D.A.T. Harper, and P.D. Ryan. 2001. *PAST: paleontological statistics software package for education and data analysis*. Palaeontologica Electronica. http://palaeo-electronica.org. Accessed 1 Jun 2021.

Hapke, C.J., E.A. Himmelstoss, M.G. Kratzmann, J.H. List, and E.R. Thieler. 2011. *National assessment of shoreline change: historical shoreline change along the New England and Mid-Atlantic coasts*. U.S. Geological Survey Open-File Report 2010–1118. https://doi.org/10.3133/ofr20101118.

Hawkes, A.D., and B.P. Horton. 2012. Sedimentary record of storm deposits from Hurricane Ike, Galveston and San Luis Islands, Texas. *Geomorphology* 171–172: 180–189. https://doi.org/10.1016/j.geomorph.2012.05.017.

Hollis, R.J., D.J. Wallace, M.D. Miner, N.S. Gal, C. Dike, and J.G. Flocks. 2019. Late Quaternary evolution and stratigraphic framework influence on coastal systems along the north-central Gulf of Mexico, USA. *Quaternary Science Reviews* 223: 105910. https://doi.org/10.1016/j.quascirev.2019.105910.

Hopkinson, C.S., J.T. Morris, S. Fagherazzi, W.M. Wollheim, and P.A. Raymond. 2018. Lateral marsh edge erosion as a source of sediments for vertical marsh accretion. *Journal of Geophysical Research: Biogeosciences* 123: 2444–2465.

Kemp, A.C., B.P. Horton, and S.J. Culver. 2009. Distribution of modern salt marsh foraminifera in the Albemarle-Pamlico estuarine system of North Carolina, USA: Implications for sea-level research. *Marine Micropaleontology* 72: 222–238.

Kramer, K.A. 1990. *Late pleistocene to holocene geologic evolution of the Grand Batture Headland Area, Jackson County, Mississippi*, 165. Starkville, Mississippi: Mississippi State University Master's Thesis.

Krishnaswami, S., D. Lal, J.M. Martin, and M. Meybeck. 1971. Geochronology of lake sediments. *Earth and Planetary Science Letters* 11: 407–414.

Lacy, J.R., M.R. Foster-Martinez, R.M. Allen, M.C. Ferner, and J.C. Callaway. 2020. Seasonal variation in sediment delivery across the bay-marsh interface of an estuarine salt marsh. *Journal of Geophysical Research: Oceans* 125: e2019JC015268. https://doi.org/10.1029/2019JC015268.

Lamb, G.M. 1972. Distribution of Holocene foraminifera in Mobile Bay and the effect of salinity changes. *Geological Survey of Alabama Circular* 82: 1–12.

Leonardi, N., N.K. Ganju, and S. Fagherazzi. 2016. A linear relationship between wave power and erosion determines salt-marsh

resilience to violent storms and hurricanes. *Proceedings of the National Academy of Sciences* 113: 64–68.

Liu, K., and M.L. Fearn. 1993. Lake-sediment record of late Holocene hurricane activities from coastal Alabama. *Geology* 21: 793–796.

Marot, M.E., C.G. Smith, T.A. McCloskey, S.D. Locker, N.S. Khan, and K.E.L. Smith. 2019. *Sedimentary data from Grand Bay, Alabama/Mississippi, 2014–2016*. U.S. Geological Survey data release. https://doi.org/10.5066/P9FO8R3Y.

McClenachan, G., R.E. Turner, and A.W. Tweel. 2013. Effects of oil on the rate and trajectory of Louisiana marsh shoreline erosion. *Environmental Research Letters* 8: 044030.

Milan, C.S., E.M. Swenson, R.E. Turner, and J.M. Lee. 1995. Assessment of the 137-Cs method for estimating sediment accumulation rates: Louisiana salt marshes. *Journal of Coastal Research* 11: 296–307.

Morton, R.A. 2008. Historical changes in the Mississippi-Alabama barrier-island chain and the roles of extreme storms, sea level, and human activities. *Journal of Coastal Research* 246: 1587–1600.

Nittrouer, C.A., R.W. Sternberg, R. Carpenter, and J.T. Bennett. 1979. The use of Pb-210 geochronology as a sedimentological tool: application to the Washington continental shelf. *Marine Geology* 31: 297–316.

NOAA Shoreline Website: NOAA Historical Surveys (T-Sheets). https://shoreline.noaa.gov/data/datasheets/t-sheets.html. Accessed 19 Oct 2017.

NOAA Tides and Currents Website: Datums for 8740166, Grand Bay NERR, Mississippi Sound MS. https://tidesandcurrents.noaa.gov/datums.html?datum=NAVD88&units=1&epoch=0&id=8740166&name=Grand+Bay+NERR%2C+Mississippi+Sound&state=MS. Accessed 21 Sep 2023.

Nowacki, D.J., and N.K. Ganju. 2019. Simple metrics predict salt-marsh sediment fluxes. *Geophysical Research Letters* 46: 12250–12257. https://doi.org/10.1029/2019GL083819.

Nowacki, D.J., and N.K. Ganju. 2020. Sediment dynamics of a divergent bay-marsh complex. *Estuaries and Coasts* 44: 1216–1230.

Osbourne, T.Z., and R.D. DeLaune. 2013. Soil and sediment sampling of inundated environments. *Health Physics* 51: 53–59.

Osterman, L.E., and C.G. Smith. 2012. Over 100 years of environmental change recorded by foraminifers and sediments in Mobile Bay, Alabama, Gulf of Mexico, USA. *Estuarine, Coastal and Shelf Science* 115: 345–358.

Passeri, D.L., S.C. Hagen, S.C. Medeiros, and M.V. Bilskie. 2015. Impacts of historic morphology and sea level rise on tidal hydrodynamics in a microtidal estuary (Grand Bay, Mississippi). *Continental Shelf Research* 11: 150–158.

Phillips, J.D. 1986. Coastal submergence and marsh fringe erosion. *Journal of Coastal Research* 2: 427–436.

Phleger. 1954. Ecology of foraminifera and associated micro-organisms from Mississippi sound and environs. *The Bulletin of the America Association of Petroleum Geologists* 38: 584–647.

Poppe, L.J., A.H. Eliason, J.J. Fredericks, R.R. Rendigs, D. Blackwood, and C.F. Polloni. 2000. Chapter 1: Grain-size analysis of marine sediments: methodology and data processing. In *USGS east-coast sediment analysis: procedures, database, and georeferenced displays*. U.S. Geological Survey Open-File Report 00–358. Available at https://pubs.usgs.gov/of/2000/of00%E2%80%93358/text/chapter1.htm. Accessed 1 Jun 2021.

Reed, D.J., T. Spencer, A.L. Murray, J.R. French, and L. Lynn. 1999. Marsh surface sediment deposition and the role of tidal creeks: implications for created and managed coastal marshes. *Journal of Coastal Conservation* 5: 81–90.

Robbins, J.A. 1978. Geochemical and geophysical applications of radioactive lead. In *Biogeochemistry of lead in the environment*, ed. J.O. Nriagu, 285–393. Amsterdam: Elsevier Scientific.

Robbins, J.A., and D.N. Edgington. 1975. Determination of recent sedimentation rates in Lake Michigan using Pb-210 and Cs-137. *Geochimica Et Cosmochimica Acta* 39: 285–304.

Sanford, L.P., and J. Gao. 2018. Influences of wave climate and sea level on shoreline erosion rates in the Maryland Chesapeake Bay. *Estuaries and Coasts* 41: 19–37.

Schönfeld, J., E. Alve, E. Geslin, F. Jorissen, S. Korsun, S. Spezzaferri, and members of the FOBIMO group. 2012. The FOBIMO (FOraminiferal BIo-MOnitoring) initiative- towards standardised protocol for soft-bottom benthic foraminiferal monitoring studies. *Marine Micropaleontology* 94–95: 1–13.

Schwimmer, R.A. 2001. Rates and processes of marsh shoreline erosion in Rehoboth Bay, Delaware, USA. *Journal of Coastal Research* 17: 672–683.

Scott, D.B. 1976. *Quantitative studies of marsh foraminiferal patterns in southern California and their application to Holocene stratigraphic problems*, 153–170. Maritime Sediments, Special Issue I, First International Symposium on Benthonic Foraminifera of Continental Margins, Part A, Ecology and Biology.

Scott, D.B., and F.S. Medioli. 1978. Vertical zonations of marsh foraminifera as accurate indicators of former sea-levels. *Nature* 272: 538–541.

Scott, D.B., and F.S. Medioli. 1980. Quantitative studies of marsh foraminiferal distribution in Nova Scotia: Implications for sea level studies. *Cushman Foundation for Foraminiferal Research, Special Publication* 17: 1–58.

Smilauer, P., and J. Leps. 2014. *Multivariate analysis of ecological data using CANOCO 5*. Cambridge University Press.

Smith, M.J., and R.G. Cromley. 2006. *Coastal survey maps: from historical documents to digital databases*. University of Connecticut Center for Geographic Information and Analysis (UCCGIA) Papers and Proceedings https://opencommons.uconn.edu/uccgia_papers/1. Accessed 25 Feb 2022.

Smith, C.G., L.E. Osterman, and R.Z. Poore. 2013. An examination of historical inorganic sedimentation and organic matter accumulation in several marsh types within the Mobile Bay and Mobile-Tensaw River Delta Region. *Journal of Coastal Research* 63: 68–83.

Smith, K.E.L., J.F. Terrano, N.S. Khan, C.G. Smith, and J.L. Pitchford. 2021a. Lateral shoreline erosion and shore-proximal sediment deposition on a coastal marsh from seasonal, storm, and decadal measurements. *Geomorphology* 389: 107829. https://doi.org/10.1016/j.geomorph.2021.107829.

Smith, K.E.L., J.F. Terrano, J.L. Pitchford, and M.J. Archer. 2021b. Coastal wetland shoreline change monitoring: a comparison of shorelines from high-resolution worldview satellite imagery, aerial imagery, and field surveys. *Remote Sensing* 13: 3030. https://doi.org/10.3390/rs13153030.

Stumpf, R.P. 1983. The process of sedimentation on the surface of a salt marsh. *Estuarine, Coastal and Shelf Science* 17: 495–508.

Terrano, J. 2018. *An evaluation of marsh shoreline erosion and sediment deposition in the Grand Bay National Estuarine Research Reserve, Mississippi, USA*. Graduate Theses and Dissertations available online at https://scholarcommons.usf.edu/etd/7371. Accessed 1 Jun 2021.

Terrano, J.F., K.E.L. Smith, J. Pitchford, J. McIlwain, and M. Archer. 2019. *Shoreline-change analysis for the Grand Bay National Estuarine Research Reserve, Mississippi Alabama—1848 to 2017 (ver. 2.0, February 2019)*. U.S. Geological Survey data release. https://doi.org/10.5066/P9JMA8WK.

Wacker, K.P., and G.A. Criss. 1996. *Erosional rates in the Point aux Chenes Bay area, Mississippi: 1990–1995*, 1–13. Sixtieth annual meeting of the Mississippi Academy of Sciences.

Wilson, C.A., G.M.E. Perillo, and Z.J. Hughes. 2021. Salt marsh ecogeomorphic processes and dynamics. In *Salt marshes:*

function, dynamics, and stresses, ed. D.M. Figzerald and Z.J. Hughes, 178–224. Cambridge University Press.

Yao, Q., K. Liu, and J. Ryu. 2018. Multi-proxy characterization of Hurricanes Rita and Ike storm deposits in the Rockefeller Wildlife Refuge, southwestern Louisiana. *Journal of Coastal Research* 85: 841–845. https://doi.org/10.2112/SI85-169.1.